Title

Cryo-EM structures reveal the molecular basis of receptor-initiated coxsackievirus uncoating

Permalink

https://escholarship.org/uc/item/39n2b31s

Journal

Cell Host & Microbe, 29(3)

ISSN

1931-3128

Authors

Xu, Longfa
Zheng, Qingbing
Zhu, Rui
et al.

Publication Date

2021-03-01

DOI

10.1016/j.chom.2021.01.001

Published in final edited form as:
Cell Host Microbe. 2021 March 10; 29(3): 448–462.e5. doi:10.1016/j.chom.2021.01.001.

Cryo-EM structures reveal the molecular basis of receptor-initiated coxsackievirus uncoating

Longfa Xu[1,6], **Qingbing Zheng**[1,6], **Rui Zhu**[1,6], **Zhichao Yin**[1,6], **Hai Yu**[1,6], **Yu Lin**[1], **Yuanyuan Wu**[1], **Maozhou He**[1], **Yang Huang**[1], **Yichao Jiang**[1], **Hui Sun**[1], **Zhenghui Zha**[1], **Hongwei Yang**[1], **Qiongzi Huang**[1], **Dongqing Zhang**[1], **Zhenqin Chen**[1], **Xiangzhong Ye**[4], **Jinle Han**[4], **Lisheng Yang**[4], **Che Liu**[1], **Yuqiong Que**[1], **Mujin Fang**[1], **Ying Gu**[1], **Jun Zhang**[1], **Wenxin Luo**[1], **Z. Hong Zhou**[2,3,*], **Shaowei Li**[1,*], **Tong Cheng**[1,*], **Ningshao Xia**[1,5,7,*]

[1]State Key Laboratory of Molecular Vaccinology and Molecular Diagnostics, National Institute of Diagnostics and Vaccine Development in Infectious Diseases, School of Life Sciences, School of Public Health, Xiamen University, Xiamen 361102, China

[2]California NanoSystems Institute (CNSI), UCLA, Los Angeles, CA 90095, USA

[3]Department of Microbiology, Immunology and Molecular Genetics, University of California, Los Angeles, Los Angeles, CA 90095, USA

[4]Beijing Wantai Enterprise Community Partners, Beijing 102206, China

[5]Research Unit of Frontier Technology of Structural Vaccinology, Chinese Academy of Medical Sciences, Xiamen, Fujian 361102, China

[6]These authors contributed equally

[7]Lead contact

SUMMARY

Enterovirus uncoating receptors bind at the surface depression ("canyon") that encircles each capsid vertex causing the release of a host-derived lipid called "pocket factor" that is buried in a hydrophobic pocket formed by the major viral capsid protein, VP1. Coxsackievirus and adenovirus receptor (CAR) is a universal uncoating receptor of group B coxsackieviruses (CVB). Here, we present five high-resolution cryoEM structures of CVB representing different stages of virus infection. Structural comparisons show that the CAR penetrates deeper into the canyon than other uncoating receptors, leading to a cascade of events: collapse of the VP1 hydrophobic pocket,

---

[*]Correspondence: hong.zhou@ucla.edu (Z.H.Z.), shaowei@xmu.edu.cn (S.L.), tcheng@xmu.edu.cn (T.C.), nsxia@xmu.edu.cn (N.X.).

AUTHOR CONTRIBUTIONS

L.X., Q.Z., R.Z., Z.H.Z., S.L., T.C., and N.X. contributed to the experimental design. L.X., Q.Z., R.Z., Z.H.Z., S.L., T.C., and N.X. contributed to the manuscript preparation. L.X., R.Z., Z.Y., Y.L., Y.W., Y.J., H.S., Q.H., D.Z., X.Y., J.H., L.Y., Y.Q., and M.F. contributed to the virus preparation and characteristic analysis. Z.Y., L.Y., Y.W., H.Y., and Q.H. contributed to the preparation and *in vitro* characterization of antibody. L.X., Z.Y., and C.L. performed the animal experiments. Q.Z., R.Z., H.Y., M.H., Y.H., Z.Z., Z.C., J.Z., Y.G., and W.L. contributed to the structural data collection and analysis. All authors approved the final version. All authors discussed the results and commented on the manuscript.

DECLARATION OF INTERESTS

The authors declare no competing interests.

SUPPLEMENTAL INFORMATION

Supplemental Information can be found online at https://doi.org/10.1016/j.chom.2021.01.001.

high-efficiency release of the pocket factor and viral uncoating and genome release under neutral pH, as compared with low pH. Furthermore, we identified a potent therapeutic antibody that can neutralize viral infection by interfering with virion-CAR interactions, destabilizing the capsid and inducing virion disruption. Together, these results define the structural basis of CVB cell entry and antibody neutralization.

Graphical Abstract

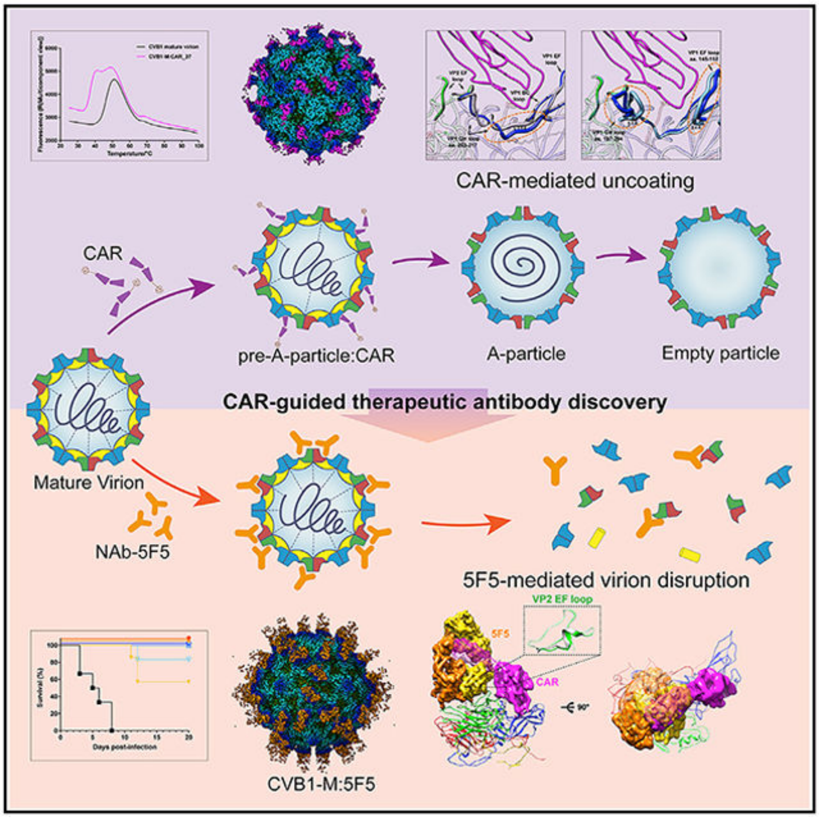

In Brief

Xu et al. present cryoEM structures that decipher the molecular mechanism of group B coxsackievirus (CVB) uncoating mediated by its receptor, CAR, under physiological conditions. Through a CAR-guided strategy, they identify a monoclonal antibody that can destabilize the capsid, disrupt the virion, and potently neutralize CVB infection *in vivo*.

INTRODUCTION

Group B coxsackieviruses (CVBs) are members of the *Picornaviridae* family and cause various potentially life-threatening inflammatory diseases in both infants and adults worldwide, with infants being particularly susceptible to generalized CVB infections (Lugo and Krogstad, 2016; Tavakoli et al., 2008). In recent years, severe outbreaks of CVB infections have been documented in Asia, Europe, and North America (Abedi et al., 2018; Centers for Disease Control and Prevention, 2010; Delogu et al., 2018; Hayakawa et al., 2019; Pauwels et al., 2012). In particular, in the United States, CVB accounts for 4 out of the top-15 most-frequently occurring enterovirus serotypes from 2014–2016 (Abedi et al., 2018). Six serotypes of CVBs (CVB1–CVB6) are significant human pathogens causing febrile illness and diseases of the heart, pancreas, and central nervous system (Huber and Ramsingh, 2004; Pollack et al., 2015; Tavakoli et al., 2008). For example, they are also among the major causative agents of viral myocarditis, and are implicated as a cause of dilated cardiomyopathy (DCM), one of the most common indications for cardiac transplantation (Pollack et al., 2015; Towbin et al., 2006). They are also implicated as environmental factors in the etiology of type 1 diabetes mellitus (T1DM) through persistent infection and cause inflammation of pancreatic β-cells (Dunne et al., 2019; Hyöty et al., 2018; Krogvold et al., 2015; Richardson and Morgan, 2018). However, there is no cure or vaccine against CVB infections yet.

Picornaviruses infect host cells by binding to membrane receptors and undergoing receptor-mediated endocytosis (Baggen et al., 2018b; Marsh and Helenius, 2006). Numerous enterovirus receptors have been identified, and are classified into either attachment or uncoating receptors based on their involvement in cell entry or genome release, respectively (Baggen et al., 2018a; Bergelson et al., 1994; He et al., 2001; Mendelsohn et al., 1989; Sun et al., 2020; Zhang et al., 2008; Zhao et al., 2019, 2020, Zhou et al., 2019). Attachment receptors facilitate virus attachment to host cells and promote virus uptake. Uncoating receptors induce conformational changes in the viral capsid and mediate viral uncoating (Zhao et al., 2019). Specifically, they bind at the surface depression (“canyon”) that encircles each icosahedral 5-fold vertex of the capsid and cause the mature virion to release a host-derived lipid moiety, called “pocket factor” that is buried in a hydrophobic pocket formed by the major viral capsid protein, VP1, beneath the canyon (Plevka et al., 2012; Wang et al., 2012). Loss of the pocket factor causes the pocket to collapse, followed by opening of a channel near the icosahedral 2-fold axis, and consequently the formation of an expanded uncoating intermediate, known as the “A-particle” (Ren et al., 2013; Xu et al., 2017). Notably, uncoating of most enteroviruses during cell entry requires both binding to a receptor and exposure to low pH (Zhao et al., 2019; Zhou et al., 2019).

Despite numerous prior structural studies, the mechanism of receptor-mediated uncoating remains elusive. Uncoating receptors are used by many non-enveloped viruses: scavenger receptor B2 (SCARB2) for enterovirus 71 (EV71) and coxsackievirus A16 (CVA16); kringle-containing transmembrane protein 1 (KRM1) for CVA10, and some of the group A enteroviruses; coxsackievirus and adenovirus receptor (CAR) and human neonatal Fc receptor (FcRn) for group B enteroviruses; CD155 for poliovirus; and intercellular adhesion molecule-1 (ICAM-1) for CVA21 and CVA24 (Bergelson et al., 1997; Greve et al., 1989; Mendelsohn et al., 1989; Nishimura et al., 2009; Staring et al., 2018; Yamayoshi et al., 2009; Zhao et al., 2019). Moderate resolution structures of several enteroviruses in complex with receptor have been determined by cryogenic electron microscopy (cryoEM), including CVB3, CVA21, CVA24, and poliovirus (Baggen et al., 2018a; He et al., 2001; Organtini et al., 2014; Strauss et al., 2015; Zhang et al., 2008), but limited resolutions have prevented mechanistic understanding. Recently, higher-resolution structures have also been inconclusive. For example, initial attachment complex of SCARB2-EV71 at low pH (5.1) showed an unexpanded capsid, indistinguishable from the mature virus (Zhou et al., 2019) and KRM1 binding minimally affected CVA10 mature capsid (Zhao et al., 2020). By contrast, the structure of the FcRn-Echo 6 complex revealed that FcRn binding transformed virions into an uncoating intermediate state under acidic conditions (Zhao et al., 2019).

CAR, a cell adhesion molecule found in tight junctions, plays a crucial role in CVB-related pathology (Kallewaard et al., 2009; Vehik et al., 2019). CAR was previously identified as a universal uncoating receptor for CVBs (Bergelson et al., 1997; He et al., 2001). Previous low-resolution cryoEM structures of CAR bound to CVB3 (22 and 9 Å) suggested that CAR binding could catalyze viral conformational changes, resulting in the formation of non-infectious A-particles at pH 6.0 (He et al., 2001; Organtini et al., 2014). However, due to unavailability of a high-resolution structure for CVB in complex with CAR, it remains unclear how CAR-mediated uncoating relates to that of the aforementioned receptors. Because receptor binding sites can be targeted for neutralizing antibodies (nAbs) design (He et al., 2020; Wang et al., 2017; Zheng et al., 2019; Zhu et al., 2018), high-resolution knowledge and mechanistic understanding of CAR-mediated uncoating will facilitate the development of antiviral therapeutics and the optimization of drug candidates.

In this study, we set out to systematically identify the molecular basis for CVB uncoating through CAR binding. We have determined five high-resolution cryoEM structures of CAR engaged with CVB that represent various stages of viral infection: the CVB1 mature virion, the CAR-decorated transition-state particle (named as pre-A-particle) at both low and physiological temperatures, the CAR-triggered A-particle, and the empty particle. CAR exhibited potent uncoating efficiency: its binding triggered the transformation of mature virions into A-particles and even into empty particles under neutral conditions *in vitro*. Moreover, through a CAR-guided strategy, we identified 5F5, a potent nAb that efficiently blocks viral infection by interfering with virion-CAR interaction. Remarkably, nAb 5F5 can cause capsid destabilization and can neutralize CVB1 by antibody-mediated virion disruption. Our findings provide insight into the structural basis and dynamics of virus entry and disruptive neutralization, demonstrate the high therapeutic potential of nAb 5F5, and should inform rational design of prophylactic and therapeutic countermeasures against diseases caused by CVB and other picornaviruses.

RESULTS

Structural transformation of CVB1 mature virion upon CAR binding

The clinical CVB1 strain, CVB1-301 (GenBank accession no. MT129657), was cultivated and purified from human rhabdomyosarcoma (RD) cells. Two bands were observed in the 15% to 45% (w/v) sucrose gradient of the ultracentrifugation. SDS-PAGE showed that the particles in the bottom band (lane 1) comprised four capsid proteins, VP1–VP4, whereas those in the top band (lane 2) showed no trace of VP4 (Figure S1A). Electron microscopy images of the negative-stained sample further confirmed the presence of genome material within the particles in the bottom band but not in the top band (Figures S1B and S1C). Taken together, these characteristics suggest that the particles in the bottom and top bands correspond to CVB1 mature virions (CVB1-M) and empty particles (CVB1-E), respectively.

We then determined the cryoEM structures of both CVB1-M and CVB1-E to resolutions of 3.2 and 3.4 Å, respectively (Figures 1A, 1B, S1D-S1G, S2A, and S2B; Table S1). The near-atomic structures of CVB1-M and CVB1-E were similar to those of other enteroviruses. The electronic density maps of CVB1-M and CVB1-E both revealed a pseudo $T = 3$ icosahedral capsid structure with a maximum diameter along the 5-fold axis of ~336 and ~350 Å, respectively (Figures 1A and 1B). To investigate how CAR mediates CVB1 uncoating, the complexes of CAR bound to CVB1-M were incubated at either a low temperature (4°C, CVB1-M:CAR_4) or physiological temperature (37°C, CVB1-M:CAR_37) under neutral conditions (pH 7.4) and were then flash cooled for cryoEM data collection. As revealed by 2D and 3D classifications (Figures S1H-S1K), the density of CAR while decorating the mature virion at 4°C was less than that at 37°C, suggesting the binding of CAR at the low temperature is unsaturated. Furthermore, CAR binding at 37°C predominantly formed two types of particles: CAR-decorated complex and CAR-triggered A-particle, with a ratio of 1:8. Of note, the CAR-triggered A-particle was only found at physiological 37°C, not at 4°C. In addition, a minority of empty particles (2.6%) was also obtained at physiological 37°C, suggesting that CAR can directly trigger viral uncoating and genome release at neutral pH; this differentiates CAR from the uncoating receptors of other enteroviruses. The A-particles and empty particles derived from the CVB1-M:CAR complex showed no evidence of bound CAR.

The subsequent 3D reconstruction of CVB1-M:CAR_4, CVB1-M:CAR_37, and CAR-triggered A-particle yielded final density maps at resolutions of 3.8, 3.6, and 3.8 Å, respectively (Figures 1C, 1D, S1H-S1K, S2C-S2E, and S3A-S3C; Video S1; Table S1). The maps of CVB1-M:CAR_4 and CVB1-M:CAR_37 are essentially identical, with a map correlation coefficient of 0.97 (Figures 1C and S3A-S3C). CAR binds to CVB1-M in its canyon region, and the viral particle in the CAR-decorated complex is structurally similar to the mature virion, with a closed 2-fold channel, a similar inner genome organization, and an identical diameter. The CAR-triggered A-particles share an expanded capsid structure essentially identical to those of the empty particles (map correlation coefficient of 0.95); the channels at the icosahedral 2-fold axes are open and the inner genome appears re-organized (Figures 1B and 1D). The density maps for all of these particles show clear delineation of the protein backbones, and the side chains of most of the amino acid (aa) residues are resolved, which allowed us to build their atomic models (Figure 1E).

Next, we sought direct evidence for receptor-mediated destabilization of the CVB1 virus using particle stability thermal release assays (PaSTRy). Binding of CAR to CVB1-M significantly increased dye accessibility to the genomic RNA, with prominent fluorescence detected at a lower temperature (about 37°C) than that required for the untreated mature virions (at about 52°C) (Figure 1F). These observations show that CAR is a highly efficient uncoating receptor for CVB1 entry and can mediate viral uncoating under neutral conditions *in vitro*. Moreover, cell-based RT-PCR and neutralization assays were used to quantify the blocking (neutralizing) efficacy of soluble CAR against viral particle attachment to host cells (Figures 1G and 1H). When pre-mixed with CVB1-M *in vitro*, CAR was able to significantly reduce the amount of virus bound to host cells and block infection, with the blocking efficiency shown to be concentration dependent (Figures 1G and 1H). In contrast, soluble CAR was unable to inhibit virus attachment and infection in the post-attachment mode (Figures 1G and 1H). Thus, the cell-based inhibition studies further verified that the CAR-decorated complex and CAR-triggered A-particle cannot bind to cellular receptors and efficiently infect cells, indicating that the free A-particles and empty particles are the remnants of a non-infectious, uncoated virus.

Molecular basis for CVB1 structural transformation triggered by CAR binding

Like other picornaviruses, in our CVB1-M structure, we observed that a lipid molecule known as the pocket factor was well accommodated in the pocket formed by VP1 beneath the canyon that regulates viral stability (Figure 2A). Unlike the situation of CVB1-M, the pocket factor was released in both the CAR-decorated complex and the CAR-triggered A-particle (Figures 2B and 2C). Binding of CAR to the canyon region of CVB1 led to partial collapse of the pocket, causing the canyon to become narrower (Figures 2D and 2E). By comparison, the A-particle triggered by CAR binding had a fully collapsed pocket and a deeper canyon (Figure 2F). Superimposed models show that the binding of CAR to the mature virion induces a significant conformational change in the VP1 GH loop (Figures 2G and 2H): the VP1 GH loop moves down by ~2.5 Å and two key residues—N211 and M213—move into the space of the original pocket factor. Such a downward shift of the GHloop causes clashes with the pocket factor and results in its release (Figures 2G, 2I, and S3D-S3L; Video S2).

Aside from the release of the pocket factor, the CAR-decorated CVB1 particle is structurally similar to the mature virion (RMSD of 0.45 Å of all 806 aligned Cα positions in one protomer) but different from the CAR-triggered A-particle (RMSD of 1.3 Å of all 671 aligned Cα positions) (Figure 3A). As mentioned earlier, the similarity in terms of the numerous structural features—unexpanded particle size, closed 2-fold channel, VP4 presence, and similar genome organization—suggest that the CAR-decorated viral particle represents an early intermediate state that is distinct from the classical A-particle. We thus termed this putative early intermediate state particle as “pre-A-particle.” The main structural differences among the capsids on the mature virion/pre-A-particle and the A-particle are found in the VP1 loops near the 5-fold axis (BC, DE, EF, FG, and HI loops; Figure 3B). The density map of the CAR-triggered A-particle does not have any extra density belonging to CAR, suggesting that CAR is dissociated from the viral particle during its transition from a CAR-decorated pre-A-particle to a classical A-particle.

Intriguingly, the interactions between CAR and the virion mainly involve the VP1 BC/EF/GH loops and the VP2 EF loop; among them, only GH loop aa 203–217 undergo a significant conformational change after CAR binding (Figure 3C). As mentioned above, the VP1 GH loop can act as a sensor and initiate a cascade of conformational changes, including the release of the pocket factor and the expansion of the virion to facilitate the externalization of the N terminus of VP1 and VP4, and the formation of the A-particle and empty particle (Figures 2 and 3). A similar sensor-adaptor mechanism for viral uncoating has also been proposed for EV71 (Wang et al., 2012). Of note, transition of the pre-A-particle to an A-particle is accompanied by movement of the VP1 EF loop (aa 145–152) and part of the GH loop (aa 197–204) by 2.4 and 5.3 Å, respectively (Figure 3D). Conceivably, the spatial proximity of these two loops would compress the space of the canyon region and, consequently, may cause extrusion of the bound CAR (Video S2).

We also compared the interaction features of other previously reported uncoating receptors: KRM1 for CVA10, CD155 for PV1, FcRn for Echo 6, SCARB2 for EV71, and ICAM-1 for CVA24. Similar conformational changes on the VP1 GH loop and the release of pocket factor were only observed for CD155-bound PV1 (Figures S4A-S4E). Unlike with CVB1, none of these other receptors could directly trigger the transition of the mature virions to A-particles or empty particles under neutral conditions. Previous data show that most of the receptors target the VP1 GH loop and VP2 EF loop, which are very long in sequence and play critical roles in viral uncoating (Figures S4F-S4K). Although the VP1 GH loop was previously defined as a sensor for viral uncoating (Wang et al., 2012), our CAR-decorated structure data suggest that CAR can only induce efficient viral uncoating when it approaches the deeper region of the canyon (VP1 aa 210–214, part of GH loop). This further suggests that it would be difficult for bulkier receptors to directly target this region. These structural features support the unique role of CAR in mediating pocket factor release and capsid uncoating.

Molecular details of interactions between CVB1 and CAR

CAR penetrates deep into the canyon region, with the D1 domain primarily interacting with the VP1 and VP2 of one protomer as well as the VP3 from an adjacent protomer (Figures 4A and 4B). This binding buries a total surface area of ~860 Å^2 on the virion capsid. The binding of CAR to CVB1 is mediated by five hydrogen bonds and several van der Waals contacts between the AA' sheet (aa 21–32), BC/FG loop of the D1 domain of CAR and the VP1 BC/EF/GH loops, VP2 EF loop, and VP3 GH loop from two adjacent protomers. This creates two interfaces along the rims of the canyon region (Figures 4A-4D). The AA' sheet of CAR engages at the southern rim of the canyon, making contact mainly with the EF loop of VP2 (N138, N139, and K166), while the BC loop of CAR penetrates deep into the canyon floor and forms hydrogen bonds with G147 of the VP1 EF loop and E183 of VP3 GH loop of the neighboring protomer (Figures 4B-4D). There are also strong electrostatic interactions between T24 of the AA' sheet and N139 and K166 in the VP2 EF loop (Figures 4E and 4F). Residues T24, E26, T44, and Q50 establish an elaborate hydrogen-bonding network and a charged interface with the VP1, VP2, and VP3 subunits; this comprises the core of the CAR-CVB1 interface (Figures 4B-4F). A total of 19 residues from the virus and 11 from CAR are involved in receptor interactions, with 12 of the 19 residues shown to be highly conserved across CVB group members, especially residues in the VP1 EF and GH loops (Figure S5A). Thus, it appears that CAR engages at a universal site across CVB group viruses.

CAR has also been characterized as a primary receptor for most adenovirus (AdV) serotypes. Additionally, CAR can also heterodimerize with junction adhesion molecule-like (JAML)—immune system cell signaling receptors implicated in asthma, cancer, and chronic nonhealing wounds. Previous structural studies have shown that AdV and JAML bind to CAR with similar footprints involving mainly the CD and FG loops of the D1 domain (Seiradake et al., 2006; Verdino et al., 2010). In contrast, we show that distinct residues on CAR are involved in CVB1 binding from the AA' sheet and BC and FG loops. Nonetheless, some conserved residues are found in the binding sites of both adenoviruses and CVB1, including E48 and Q50 in the BC loop, and P126 in the FG loop (Figures S5B-S5D). Notably, P126 was found to be involved in the interactions of CAR with CVB1, AdV, and JAML (Figures S5B-S5D), indicating that it might play a critical role in the CAR-mediated viral infections and other diseases.

CAR-guided discovery of a potent therapeutic antibody against CVB1

To gain further insight into the underlying biological role of CAR-CVB1 interactions, female BALB/c mice were immunized subcutaneously with the mature virions, and we screened monoclonal antibodies targeting CAR-binding sites by performing a CAR-based competitive binding assay. Purified CVB1 mature virions were coated and used to screen for CVB1-specific antibodies in the presence of soluble CAR. Antibodies with highly competitive efficiency against binding of CAR were selected and further confirmed by neutralization assay. A monoclonal antibody, referred to as 5F5, was shown to efficiently inhibit the binding of CAR to the mature virion in a concentration-dependent manner (Figure 5A). This suggests that the binding sites of 5F5 might overlap with or are adjacent to the CAR-binding region. Surface plasmon resonance (SPR) experiments showed that 5F5 binds to the mature virion with a high affinity of 22.6 ± 5.8 nM (Figure 5B). Cell-based neutralization assays further revealed that 5F5 has strong neutralizing activities, with half-maximum inhibitory concentration (IC_{50}) values of 0.11 and 1.49 μg mL^{-1} against CVB1 301 and Conn-5 strains (Figure 5C), respectively. Additionally, the CDRs of the heavy and light chains of mAb 5F5 were grafted onto human IgG1 frameworks to construct chimeric 5F5 (ch5F5). Furthermore, we modified the variable regions and constructed twelve versions of humanized 5F5 (hu5F5). We evaluated the cross-neutralization potential of these antibodies against CVB1. Remarkably, from the panel of 12 humanized 5F5 antibodies, six humanized antibodies cross-neutralized CVB1 301 and Conn-5 strains, with hu5F5-2 and hu5F5-12 showing the greatest potency (Figures 5D and 5E).

To explore the protection efficacy of 5F5 against lethal challenge with CVB1 virus *in vivo*, a single dosage of 5F5 and hu5F5-2 at 12 h were administered to 1-day-old mice after viral challenge. The mice in the control group started to show symptoms at 3 days post infection (dpi) and all animals died within 8 dpi. Full protection (100%) was observed against lethal infection in mice administered with 10 or 1 mg/kg of 5F5 and hu5F5-2, and the dosage of 0.1 mg/kg of 5F5 and hu5F5-2 also offered 60% and 80% protection against death, respectively (Figure 5F), indicating that hu5F5-2 is a candidate therapeutic agent against CVB1 infection.

Structural insight into the neutralizing mechanism of nAb 5F5

The binding profiles of 5F5 to CVB1-M were further evaluated by cryoEM. The structure of the immune complex CVB1-M:5F5 was determined at 3.2-Å resolution (Figures 6A, S1L, S1M, and S2F; Video S3; Table S1). The density map shows that 5F5 encircles the edges of the pentameric building blocks of the virus capsid around its 3-fold axes, with up to 60 copies of 5F5 able to bind to each viral particle (Figure 6A). Next, we built the atomic model of the CVB1-M:5F5 complex, which includes four major capsid proteins (VP1–VP4) and the variable domain of 5F5 Fab. Each Fab has a footprint that extends across two adjacent protomers, and its binding buries a large surface area of ~1,177 Å^2 on the capsid (Figure 6B). The 5F5 binding footprint on the CVB1 capsid is adjacent to the CAR-binding site, without overlap (Figure 6B).

To explore the structural basis for how 5F5 blocks the interaction between CVB1-M and CAR, we superimposed the complex structures of CVB1-M:5F5 and CVB1-M:CAR and found that 5F5 binding will sterically hinder CAR engagement with the virion (Figure 6C). Remarkably, both 5F5 and CAR recognize the large and prominent VP2 EF loop. We propose that 5F5 binding may cause capsid destabilization due to subtle conformational changes of the VP2 EF loop (RMSD 0.48 Å) upon the antibody binding (Figure 6C); this mimics the properties of some of the reported uncoating receptors (Zhao et al., 2019, 2020; Zhou et al., 2019) and suggests that the VP2 EF loop may also act as a sensor to trigger capsid uncoating.

Analysis of the CVB1-M:5F5 immune complex indicates that the 5F5 Fab participates mainly in the interaction through its heavy chain and binds across the VP2 BC, EF, and HI loops and the VP3 BC and HI loops from two adjacent protomers. This heavy-chain interaction accounts for ~71% of the total buried area between 5F5 and the virus. The light chain, in contrast, interacts only with the BC and EF loops of VP2 (Figure 6D). The interaction interface between 5F5 and the capsid involves 5 of the 6 complementarity-determining regions (CDRs, HCDR1–3 and LCDR1–2) and one framework region (FR, LFR3), with the formation of 7 hydrogen bonds and several van der Waals contacts with the VP2 (BC, EF, and HI loops) and VP3 (BC and HI loops) (Figure 6E; Video S3).

To further investigate the mode of antibody-mediated viral capsid destabilization, a PaSTRy assay was performed to monitor particle stability in different starting concentrations of bound 5F5. We found that the viral RNA was exposed at a lower temperature with 5F5 treatment as compared with the untreated mature virion, with genomic exposure increasing in a 5F5-concentration-dependent manner (Figure 6F). For example, a CVB1 -M:5F5 mass ratio of 1:10 or 1:50 resulted in significant increases in the exposed genomic RNA at the starting temperature and seemed to efficiently trigger transformation of the mature virion into a meta-stable state. In addition, we used a cell-based RT-PCR assay to quantify 5F5-mediated inhibition of virus particle attachment to host cells. We found that 5F5 could prevent the attachment of CVB1 to the cell surface but could not dislodge any virus that had already bound to the cell surface (Figure 6G). We further performed pre- and post-attachment neutralization assays to investigate whether 5F5 could neutralize the virus before or after virus binding to the cell surface. 5F5 could neutralize viruses in a post-attachment manner with an IC_{50} value of 3.11 μg mL^{-1}, but this was less efficient than the neutralization observed in the pre-attachment manner (0.02 μg mL^{-1}) (Figure 6H). Together, these findings indicate that 5F5 can block viral entry at multiple stages of viral infection and could be a potent therapeutic or a potential prophylactic agent against CVB1.

Uncoating efficiency of CAR and capsid-disruption potential of 5F5

To test whether CAR or 5F5 binding facilitates CVB1 uncoating or capsid disruption, we incubated mature virions with soluble CAR (CVB1-M:CAR mass ratio = 1:1) or Fab 5F5 (CVB1-M:5F5 mass ratio = 1:10) at 37°C under neutral conditions for 10 and 120 min and compared the virion morphologies by negative-staining electron microscopy. CVB1 mature virion alone, which served as a control, did not display significant changes under either incubation time (Figure 7A). By contrast, in the presence of CAR, a substantial proportion of viral particles transformed into A-particles and empty particles. The proportion of empty particles increased with a longer incubation time (Figures 7A and 7B). This observation further confirms that CAR binding to CVB1 results in highly efficient viral uncoating without the need for a low pH environment. Unexpectedly, in the case of 5F5, both incubation times led to a significant decrease in the total amount of viral particles (Figures 7A and 7C), indicating that 5F5 binding disrupted capsid integrity, as also confirmed by cryoEM analysis of the immune complex (CVB1-M:5F5 mass ratio = 1:10) that showed disappearance of intact virions after incubation for 2 h (Figures S6A and S6B). 2D classification and 3D reconstruction of resulting small particles revealed a low-resolution structure with a recognizable Fab bound to a protein subunit, which may be ascribed to the viral capsid protein (Figures S6C and S6D); these results suggest that binding of 5F5 indeed induced subunit dissociation, leading to disruption of the CVB1 virions.

Comparison of the atomic structures of the two interacting protomers (termed as protomer A and B) in CVB1-M:5F5 and A-particle offers an insight into this potent uncoating effect of 5F5 binding. Aligning the two structures based on protomer A—which is mainly involved in 5F5 binding—shows that expansion of the capsid during the transition of the mature virion to an A-particle, resulted in a slight upward rotation (~4.5°) of the adjacent protomer (protomer B) from the A-particle as compared with that of CVB1-M:5F5 (Figure 7D). In particular, the VP3 BC loop in protomer B of the A-particle shifts upward by ~3°, and this alters the conformation of the 5F5 binding site, indicating that the binding of 5F5 on the mature virion may encumber A-particle transformation. Thus, the two competing consequences of 5F5 binding to the mature virion—viral capsid destabilization (i.e., the tendency to form a meta-stable A-particle) and structural transformation blockage—may have ultimately induced the observed capsid disruption.

DISCUSSION

In this work, by comparing five high-resolution cryoEM structures, we unambiguously show that binding of CAR to CVB1 triggers a cascade of structural changes, transforming the mature virions to A-particles and even empty particles at neutral pH. Likewise, antibody 5F5 raised by CAR competition can efficiently block virus binding to CAR and induce capsid disruption. The high uncoating efficiency of CAR and efficient capsid-disruption potential of 5F5 point to a model of CVB1 infection by which virus binding to CAR triggers coxsackievirus uncoating at either the cell membrane or at early stages within the endosome (Figure S7). Furthermore, results from our structure-guided biochemistry assays suggest that, following capsid conversions upon CAR binding, only membrane-bound A-particle, rather than free A-particle, is infectious (Figure 1H). Previous studies have demonstrated that the externalization of VP4 and N-terminal of VP1 accompanied by the transformation of A-particles during viral infection may act as anchors and then puncture the membrane, creating a pore through which the viral RNA genome gains entry into the cytoplasm (Fricks and Hogle, 1990; Li et al., 1994; Panjwani et al., 2014). The externalized VP4 and N terminus of VP1 may similarly be critical to coxsackievirus infection, and CAR-mediated uncoating of membrane-bound virions may an analogous mechanism to release viral genomic RNA into the cytoplasm (Figure S7). Overall, the near-atomic-resolution structures presented here offer a full picture for understanding CAR-mediated coxsackievirus particle transformation and uncoating process.

After receptor attachment, capsid uncoating and genome release are two critical steps in the life cycle of most non-enveloped viruses, such as the picornavirus presented in this study. Analysis of the available enterovirus-receptor complexes (e.g., EV71, CVA10, PV-1, CVA24, and Echo 6) reveals distinctive patterns of virus entry mediated by uncoating receptors. All of the receptors in these studies bind to or around the canyon regions, including the VP1 BC, DE, EF, GH loops, and the C terminus; the VP2 EF loop; and the VP3 AB and GH loops, and the C terminus (Figures S4F-S4K) (Baggen et al., 2018a; Strauss et al., 2015; Zhao et al., 2019, 2020; Zhou et al., 2019). Among enteroviruses, these loops are not only the most diverse in terms of sequence, length, and structure but they also often constitute viral neutralization epitopes. Binding of KRM1 to CVA10 appears to directly trigger uncoating by conversion of a small amount of mature virions to A-particles (only ~10% of undecorated A-particles) at pH 8.0 (Zhao et al., 2020). Binding of CD155 to PV-1 dislodges the pocket factor and induces minor conformational changes on some residues at the pocket region, whereas particle types essentially do not change (Figures S4A-S4E; Strauss et al., 2015). In contrast, among the FcRn-, SCARB2-, and ICAM-1-bound viruses (Figures S4A-S4E), the pocket factor is retained and no significant structural rearrangement was observed to the viral proteins (Baggen et al., 2018a; Zhao et al., 2019, Zhou et al., 2019). For these latter receptors, pH-induced conformational changes are thought to act in concert to help trigger uncoating. On the other hand, most of the identified uncoating receptors of enteroviruses that target the surrounding canyon region (e.g., KRM1, FcRn, PVR, and ICAM-1) have relatively large footprints (1,200–1,600 Å^2) on the viral surface and are comparable to the footprint of 5F5. It is believed that bulkier receptors, such as KRM1 and SCARB2, are blocked from penetrating the narrow canyon region, whereas CAR, with a slender D1 domain, can span the viral canyon with a smaller footprint (~860 Å^2) and thus penetrate relatively deeper into the canyon to contact the canyon floor via the VP1 EF and GH loops, VP2 EF loop, and VP3 GH loop. The AA’ sheet and the BC and FG loops of D1 domain interact directly with the sensitive VP1 GH loop (aa 203–217) and drive highly efficient uncoating. Thus, the mode of receptor attachment revealed in the CVB1-CAR complex in this study is unique and represents a mechanism of viral uncoating under neutral condition.

CAR is an essential multifunctional cellular protein that serves as the primary cellular receptor for CVB and most adenovirus serotypes and is also involved in cell adhesion, immune cell activation, and signaling (Bergelson et al., 1997; Excoffon, 2020; Verdino et al., 2010). A large-scale study of known eukaryotic DNA and RNA viruses in stool samples of children showed that children with prolonged shedding of CVB were more likely to develop islet autoimmunity (Vehik et al., 2019). Furthermore, CAR-mediated CVB1 infection may induce inflammation and tissue damage, with enhanced *CAR* expression found in the pancreatic tissue of patients with islet autoimmunity as well those with T1DM (Hodik et al., 2016; Vehik et al., 2019). Therefore, targeting both the CAR-binding sites on CVB1 and the CAR-mediated uncoating stage would be a promising strategy against CVB infection and its ensuing complications. Our structures show that CAR penetrates deep into the viral canyon floor and makes direct contact with two major domains: (1) the VP2 EF loop, which is located at the southern rim of the canyon and can probably be targeted by a neutralizing antibody, as revealed in other enteroviruses; (2) the VP1 GH loop, which is located on the canyon floor and inaccessible for blunt antibodies (Rossmann et al., 1985). Previous studies have also shown that the VP2 EF loop, referred to as the “puff region,” marks a large region of contact between other enteroviruses and their uncoating receptors (Baggen et al., 2018a; Zhao et al., 2019, 2020; Zhou et al., 2019). The VP2 EF loop lies in a protruding hydrophilic loop region that is also a major neutralization site. Therefore, structural knowledge of the VP2 EF loop is essential for understanding the mechanisms of viral uncoating and infection (Xu et al., 2014; Zhou et al., 2019). Indeed, the potent nAb 5F5 we raised by CAR competition targets mainly the VP2 EF loop and interferes with the virion/CAR interactions by steric hindrance. Intriguingly, 5F5 caused capsid destabilization by mimicking the properties of uncoating receptors and triggered slight conformational changes in the VP2 EF loop, leading to viral disruption.

In summary, our study offers insights into the mechanisms of highly efficient capsid uncoating and genome release of coxsackievirus upon binding to CAR under neutral conditions. By generating antibody 5F5 and characterizing its mode of actions, it also showcases a successful strategy for receptor-guided discovery of therapeutic antibodies. We show that 5F5 neutralizes coxsackieviruses by partial receptor mimicry, causing virion disruption. The plethora of knowledge on the uncoating receptor and the neutralizing antibody should inform therapeutic and prophylactic strategies against this and other picornaviruses.

STAR★METHODS

RESOURCE AVAILABILITY

Lead contact—Further information and requests for resources and reagents should be directed to and will be fulfilled by the Lead Contact, Ningshao Xia (nsxia@xmu.edu.cn).

Materials availability—All unique/stable reagents generated in this study are available from the Lead Contact with a completed Materials Transfer Agreement.

Data and code availability—The cryoEM density maps and corresponding atomic coordinates have been deposited in the Electron Microscopy Data Bank (EMDB) and Protein Bank (PDB), respectively. The accession codes are: CVB1-M (EMD-30805, PDB: 7DPF); CVB1-E (EMD-30806, PDB: 7DPG); CVB1-M:CAR_4 (EMD-30812, PDB: 7DPZ); CVB1-M:CAR_37 (EMD-30813, PDB: 7DQ1); CVB1-A (EMD-30814, PDB: 7DQ4); CVB1-M:5F5 (EMD-30815, PDB: 7DQ7).

EXPERIMENTAL MODEL AND SUBJECT DETAILS

Cell lines—Human rhabdomyosarcoma (RD) cells were obtained from the American Type Culture Collection (ATCC, CCL-136) and maintained in minimal essential medium (MEM, Gibco) supplemented with 10% fetal bovine serum (FBS, Gibco). Expi293F™ cells were obtained from Invitrogen and maintained in FreeStyle™ 293 expression medium (Gibco).

Viruses—The CVB1 301 strain (GenBank accession no. MT129657) was isolated from a HFMD clinical specimen in Fujian, China. The CVB1 Conn-5 strain (GenBank accession no. AJ295196) was obtained from the ATCC (VR-28™). Viruses were propagated on RD cells, and the supernatant was harvested and stored in aliquots at −80°C in our laboratory. The CVB1 Conn-5 strain was used only in the *in vitro* micro-neutralization assay. Virus production was titrated by plaque assay using RD cells.

Mice—BALB/c mice were obtained from the Slac Laboratory Animal Co., Shanghai, China. All mice were maintained in a specific-pathogenfree (SPF) facility of Xiamen University. For infection studies, mice were maintained in animal biosafety level 2 (ASBL2) facility at 23°C. All mice were allowed free access to sterilized water and irradiated diet, and provided with a 12 h light-dark cycle. Animal protocols were performed in accordance with the guidelines of the Xiamen University Institutional Committee for the Care and Use of Laboratory Animals, and approved by the Xiamen University Laboratory Animal Center (approval code: XMULAC20160049). Details of the mouse information can be found in the "Screening and preparation of antibodies" and "*In vivo* protection assay".

METHODS DETAILS

Virus production and purification—Isolated CVB1 was grown in RD cells at a multiplicity of infection (MOI) of 0.1 at 37°C for 72 h. After infection, the virus was centrifuged at 6,000 ×*g* for 30 min to remove cell debris and precipitated using 6% (w/v) polyethylene glycol (PEG) 6,000 and 0.3 M NaCl in PBS at 4°C overnight. After centrifugation, the virus was resuspended in PBS and then sedimented through a linear 15% to 45% (w/v) sucrose density gradient at 120,000 ×*g* for 3.5 h by a Beckman SW41 Ti rotor at 4°C. Two fractions were independently collected and dialyzed against PBS, and then concentrated by an Ultra-4 centrifugal concentrator (100 kDa, Millipore). The protein composition was analyzed by SDS-PAGE. The quantity and quality of CVB1 particles were assessed by negative-staining transmission electron microscopy.

Expression and purification of CAR proteins—The human CAR ectodomain, residues 20-237 (GenBank accession No. P78310), was cloned into a PTT5 vector with a signal peptide at the N terminus and a human IgG1 Fc region at the C terminus. The plasmid expressing the human CAR-Fc protein was transfected into Expi293F™ cells using PEI. After expression, the supernatant was collected and purified by protein A chromatography (Bestchrom). The soluble CAR proteins were dialyzed against PBS, and then concentrated by an Ultra-15 centrifugal concentrator (10 kDa, Millipore).

Screening and preparation of antibodies—To obtain anti-CVB1 monoclonal antibodies (mAbs), female BALB/c mice (6-8 weeks age) were immunized subcutaneously with CVB1 mature virions emulsified in complete Freund's adjuvant and boosted twice at 2-week intervals in incomplete Freund's adjuvant. Then, splenocytes were isolated and fused with Sp2/0 myeloma cells, and the hybridoma cell lines were further generated and screened by a CAR-based competitive ELISA and micro-neutralization assay. Antibodies were purified from ascitic fluid using protein A chromatography (Bestchrom) and dialyzed against PBS.

For the CAR-based competitive ELISA, 96-well ELISA plates were coated with anti-CVB1 mAb 8A10 (200 ng per well) at 4°C overnight and saturated with a blocking buffer (PBS supplemented with 0.25% casein and 1% gelatin) at 37°C for 2 h. The purified CVB1 mature virions (50 ng per well) were first incubated. The test antibodies were incubated simultaneously with the soluble CAR (2 μg mL^{-1}) in blocking buffer. Then, the soluble CAR was detected with horseradish peroxidase-conjugated goat anti-human (GAH-HRP; 1:5,000 dilution) IgG antibody at 37°C for 30 min. For color development, after five washes with PBST buffer (0.05% Tween-20 in PBS), the wells were incubated with a solution of TMB at 37°C for 15 min, and the reaction was terminated with 2 M H_2SO_4. Wells with no test antibodies were the control. The optical densities (OD) were converted to percentage inhibition (PI) values using the following formula: PI (%) = 100 - [($OD_{sample}/OD_{control}$) × 100].

Chimeric 5F5 (ch5F5) and humanized 5F5 (hu5F5) antibodies construction and expression—Based on human homologs of 5F5, CDR sequences of both heavy and light chains of 5F5 were grafted into the human IgG1 expression vector pTT5 (YouBio, CN) with heavy chain and kappa chain constant region to construct chimeric antibody ch5F5. In addition, from three heavy chain and four light chain designs, twelve versions of humanized 5F5 were constructed and the modified variable regions were subcloned into the same vectors. To generate these full-length hIgG1 antibodies, Expi293F™ cells were co-transfected transiently with the two expression plasmids at a 1:1 ratio using PEI and cultured for 7 days. Antibody IgG1 was purified from culture supernatants by using protein A affinity chromatography (General Electric Company, Pittsburgh, PA).

Production of Fab fragments—To obtain the Fab fragment of the Ab-5F5, the antibody was digested with papain at 1 ‰ (w/w) in 20 mM PB (pH 7.0) buffer, containing 30 mM L-Cys and 50 mM EDTA at 37°C for 10 h. After terminating the reaction with 30 mM iodoacetamide, the Fab fragments were purified using DEAE chromatography (TOSOH) and dialyzed against PBS. The sequences of the variable domains of the heavy and light chains were sequenced by PCR amplification.

PaSTRy assay—Thermofluor experiments were performed with a MX3005p RT-PCR instrument (Agilent), as previously described (Walter et al., 2012). Briefly, the green fluorescent dye SYTO® 9 (Thermo Fisher) was used to detect the presence of exposed RNA. Each 50 μL reaction mixture was set up in thin-waled PCR plates, containing 1 μg of the CVB1 mature virion and 5 μM of fluorescent dye in PBS. The fluorescence level was recorded in triplicate at 0.5°C intervals from 25°C to 99°C. In addition, a similar assay was performed for the virus:CAR and virus:5F5 complexes with 1 μg of the CVB1 mature virion pre-incubated with either 1 μg of soluble CAR protein or various concentrations of the Fab-5F5 at 37°C for 10 min.

Pre- and post-attachment inhibition assays—The attachment inhibition assays were conducted as previously described (Xu et al., 2017). In brief, for the pre-attachment inhibition assays, serially 10-fold-diluted CAR or Ab-5F5 was incubated with free CVB1 at 4°C for 1 h, and then added to the pre-seeded RD cells and incubated at 4 °C for 1 h. For post-attachment inhibition assays, the cells were first incubated with CVB1 at 4 °C for 1 h, and then washed three times with cold PBS. Serially diluted CAR or Ab-5F5 was subsequently added and incubated for at 4 °C 1 h. Unbound virus was removed by three washes with cold PBS. Total cellular RNA was extracted using the QIAamp Mini Viral RNA Extraction Kit (Qiagen). The amount of cell-bound virus RNA was determined by quantitative real-time RT-PCR using a pair of specific forward (5’-CTACCACTCACGGTCCGAATCGT-3’) and reverse primers (5’-TGAGTTRTTRGTGTATGTGGCATAGT-3’) and a fluorescence probe (5’-FAM-CCTGTGCCGGTCTGCCTGTG-BHQ-2-3’). Analysis of the relative levels of CVB1 RNA in the different samples was performed by the comparative 2-ΔΔCT method (Livak and Schmittgen, 2001).

***In vitro* neutralization assays—**RD cells were seeded into 96-well plates at 1×10^4 cells per well and then treated by one of the following three assays. For the micro-neutralization assay, serially 2-fold-diluted Ab-5F5 and twelve versions of hu5F5 (initial concentration of 1 mg mL^{-1}) were diluted serially 2-fold from 1:64 to 1:65,536 and incubated with an equal volume of CVB1 strains 301 or Conn-5 (100 $TCID_{50}$) at 37°C for 1 h, and then added to the pre-seeded cell plates. For the pre-attachment neutralization assay, serially 2-fold-diluted CAR or 5-fold-diluted Ab-5F5 was incubated with CVB1 301 (100 $TCID_{50}$) at 37°C for 1 h, and then added to the pre-seeded cell plates at 4° C for 1 h. For the post-attachment neutralization assay, CVB1 301 (100 $TCID_{50}$) was added to the pre-seeded cell plates and incubated at 4°C for 1 h. Serially 2-fold-diluted CAR or 5-fold-diluted Ab-5F5 was subsequently added to the virus/cell plates. For both the pre- and post-attachment neutralization assays, the initial concentration of CAR was 0.01 mg mL^{-1} and that of Ab-5F5 was 0.1 mg mL^{-1}. The 96-well plates were finally incubated at 37°C for 3-5 days. The neutralization titers were the averages of the triplicate readings calculated based on the highest dilution in over 50% cytopathic effect (CPE).

Competitive ELISA—The 5F5 blocking-competitive assay was performed according to the CAR-based competitive ELISA. Briefly, serially 10-fold-diluted Ab-5F5 (initial concentration of 0.2 mg mL^{-1}) was first added into the wells and incubated at 37°C for 30 min. The CAR protein at 2 μg mL^{-1} was then added and incubated at 37°C for 30 min. After five washes with PBST buffer, the soluble CAR was detected with the GAH-HRP IgG antibody. The absorbance was measured at A450/620 nm, and PI values were then calculated.

Surface plasmon resonance (SPR) assay—The binding affinity of Ab-5F5 to the CVB1 mature virion was analyzed by SPR using a BIAcore 8K instrument (GE Healthcare). The purified antibodies were directly immobilized onto a Protein A biosensor chip (GE Healthcare). Subsequently, serially 2-fold diluted mature virions were flowed over the chip surface. The chip was finally regenerated with a 10 nM glycine buffer (pH 1.5). The resulting data were analyzed and calculated using a global fit model using the BIAcore Insight Evaluation Version 1.0 software.

In vivo protection assay—To evaluate the therapeutic efficacy of Ab-5F5 and hu5F5-2 *in vivo*, one-day-old BALB/c mice (n = 6-8) were first challenged with 10 $TCID_{50}$ CVB1 delivered by intraperitoneal (i.p.) injection. At 12 h later, Ab-5F5 and hu5F5-2 was i.p. injected at doses of 10, 1, or 0.1 μg per gram body weight. The mice in the control group were treated with PBS buffer via the same route. All mice were monitored daily until 20 days post-infection.

Negative-staining transmission electron microscopy—Purified CVB1 mature virions were mixed with or without recombinant CAR proteins or 5F5 Fab fragments at 37°C for 10 min or 120 min. The CVB1 particles and complexes were then deposited onto 200-mesh carbon-coated grids for 1 min. The grids were washed twice with double distilled water and then immediately negatively stained with 2% phosphotungstic acid (pH 6.4) for 30 s. Grids were examined and imaged with an FEI Tecnai T12 transmission electron microscope at 25,000× magnification.

CryoEM sample preparation and data collection—The CVB1:CAR complex was prepared by mixing CVB1 mature virions with recombinant CAR proteins at a mass ratio of 1:1 at 4°C or 37°C for 10 min. For the CVB1:5F5 immune complex, the 5F5 Fab fragment was incubated with the CVB1 mature virion at a mass ratio of 1:10 (CVB1:5F5) at 37°C for 10 min or 120 min. Aliquots (3 μL) of purified CVB1 particles or complexes were deposited onto fresh glow-discharged holey carbon Quantifoil Cu grids (R2/2, 200 mesh, Quantifoil Micro Tools). Grids were blotted for 6 s at 100% relative humidity and 6°C for plunge-freezing (Vitrobot Mark IV, FEI) in liquid ethane cooled by liquid nitrogen. CryoEM datasets were recorded on Falcon-2 or -3 direct electron detectors at a nominal magnification of 93,000×, corresponding to a pixel size of 1.128 Å or 1.12 Å, respectively. For each movie, the total electron dose was about 25 $e^-/Å^2$, which was fractionated into 17 frames (Falcon-2) or 39 frames (Falcon-3) with an exposure time of 1 s. Data were automatically collected using FEI EPU software.

Image processing and three-dimensional reconstruction—Frames of each movie were aligned and averaged using MotionCorr2 (Zheng et al., 2017) and the contrast transfer function parameters were determined with Gctf (Zhang, 2016). Micrographs with excessive drift or astigmatism were discarded before reconstruction. Particles were automatically picked and screened using Gautomatch (https://www2.mrc-lmb.cam.ac.uk/research/locally-developed-software/zhang-software/#gauto) or Autopick session of software Relion 2.1 (Kimanius et al., 2016) or cryoSPARC 2.4.2 (Punjani et al., 2017). The initial 3D models of each dataset were generated with a random model method using AUTO3DEM (Yan et al., 2007). Several rounds of reference-free 2D classification and 3D classification were performed with Relion 2.1 to further select the particles for final refinement. Sorted particles were then subjected to final homogenous refinement and post-processing using Relion 2.1 or cryoSPARC 2.4.2. The final resolution was evaluated using the gold-standard Fourier shell correlation (threshold = 0.143 criterion) (Scheres and Chen, 2012). The local resolution was evaluated by ResMap (Swint-Kruse and Brown, 2005).

Model building and refinement—The X-ray crystal structure of CVB3 (PDB code: 1COV), which served as a homology model, was fitted into the segmented volume (including an asymmetric unit) of the final cryoEM density map of the CVB1 mature virion using UCSF Chimera (Pettersen et al., 2004) and rebuilt with Coot (Emsley et al., 2010). For the CVB1:CAR complexes, the structure of the CAR D1 domain (PDB code: 1F5W) was manually aligned into the cryoEM density map corresponding to the bound receptors. For the CVB1:5F5 immune complex, the initial atomic model for the variable domain of 5F5 Fab fragment was generated by homology modeling using Accelrys Discovery Studio software (https://www.3dsbiovia.com/products/collaborative-science/biovia-discovery-studio/). The structure of the CVB1 A-particle and the empty particle were built based on the structure of an A-particle (PDB code 5XS4) and an empty particle (PDB code 5XS5) of CVA6, respectively. The models were further improved using phenix.real_space_refine in PHENIX (Adams et al., 2010; Emsley et al., 2010). After refinement, the resulting models were fitted into the density of the other six neighboring protomers, which were executed as a whole for further refinement to avoid and optimize the clashes. Model statistics, including bond lengths, bond angles, all atom clashes, rotamer statistics, Ramachandran plot statistics, etc., were closely inspected with Coot during the entire process. The final atomic models were validated using Molprobity (Chen et al., 2010). Model statistics are summarized in Table S1. CAR or Fab densities in the maps were projected on a stereographic sphere using RIVEM (Xiao and Rossmann, 2007). The buried surface areas and the interactions were analyzed using PISA server (https://www.ebi.ac.uk/pdbe/pisa/) and the CCP4 (Collaborative Computational Project, Number 4, 1994) program suite with donor to acceptor distances ≤4 Å for hydrogen bonding interactions. All figures were generated with UCSF Chimera or Pymol (https://pymol.org/2/).

QUANTIFICATION AND STATISTICAL ANALYSIS

Statistical analysis was performed using GraphPad Prism 7.0. Statistical significance was calculated using the unpaired Student’s t-test (Figures 1G, 6G, and 7C) and Tukey’s multiple comparisons test (Figure 7B). Statistical significance was determined as $p < 0.05$ and is indicated by an asterisk (*) in plots: ns, non-significant, *$p < 0.05$, **$p < 0.01$, ****$p < 0.0001$. The 50% inhibitory concentration (IC_{50}) values in the neutralization assays (Figures 1H, 5C, and 6H) were calculated by nonlinear regression analysis. Statistical details of the experiments can be found in the Results and Figure legends.

Supplementary Material

Refer to Web version on PubMed Central for supplementary material.

ACKNOWLEDGMENTS

This work was supported by grants from the National Natural Science Foundation of China (no. 82072282, 81801646, 31670933 and 81991490), the National Science and Technology Major Projects for Major New Drugs Innovation and Development (no. 2018ZX09711003-005-003), the National Science and Technology Major Project of Infectious Diseases (no. 2017ZX10304402-002-003), the China Postdoctoral Science Foundation (no.

2019T120557), the Research Unit of Frontier Technology of Structural Vaccinology of Chinese Academy of Medical Sciences (no. 2019RU022) and the US National Institutes of Health (R01AI094386 to Z.H.Z.). The funders had no role in the study design, data collection and analysis, decision to publish, or preparation of the manuscript.

REFERENCES

Abedi GR, Watson JT, Nix WA, Oberste MS, and Gerber SI (2018). Enterovirus and Parechovirus surveillance - United States, 2014–2016. MMWR Morb. Mortal. Wkly. Rep 67, 515–518. [PubMed: 29746455]

Adams PD, Afonine PV, Bunkóczi G, Chen VB, Davis IW, Echols N, Headd JJ, Hung LW, Kapral GJ, Grosse-Kunstleve RW, et al. (2010). PHENIX: a comprehensive Python-based system for macromolecular structure solution. Acta Crystallogr. D Biol. Crystallogr 66, 213–221. [PubMed: 20124702]

Baggen J, Hurdiss DL, Zocher G, Mistry N, Roberts RW, Slager JJ, Guo H, van Vliet ALW, Wahedi M, Benschop K, et al. (2018a). Role of enhanced receptor engagement in the evolution of a pandemic acute hemorrhagic conjunctivitis virus. Proc. Natl. Acad. Sci. USA 115, 397–402. [PubMed: 29284752]

Baggen J, Thibaut HJ, Strating JRPM, and van Kuppeveld FJM (2018b). The life cycle of non-polio enteroviruses and how to target it. Nat. Rev. Microbiol 16, 368–381. [PubMed: 29626210]

Bergelson JM, Chan M, Solomon KR, St John NF, Lin H, and Finberg RW (1994). Decay-accelerating factor (CD55), a glycosylphosphatidylinositol-anchored complement regulatory protein, is a receptor for several echoviruses. Proc. Natl. Acad. Sci. USA 91, 6245–6248. [PubMed: 7517044]

Bergelson JM, Cunningham JA, Droguett G, Kurt-Jones EA, Krithivas A, Hong JS, Horwitz MS, Crowell RL, and Finberg RW (1997). Isolation of a common receptor for Coxsackie B viruses and adenoviruses 2 and 5. Science 275, 1320–1323. [PubMed: 9036860]

Centers for Disease Control and Prevention (2010). Nonpolio enterovirus and human Parechovirus surveillance — United States, 2006–2008. MMWR Morb. Mortal. Wkly. Rep 59, 1577–1580. [PubMed: 21150865]

Chen VB, Arendall WB 3rd, Headd JJ, Keedy DA, Immormino RM, Kapral GJ, Murray LW, Richardson JS, and Richardson DC (2010). MolProbity: all-atom structure validation for macromolecular crystallography. Acta Crystallogr. D Biol. Crystallogr 66, 12–21. [PubMed: 20057044]

Collaborative Computational Project, Number 4 (1994). The CCP4 suite: programs for protein crystallography. Acta Crystallogr. D Biol. Crystallogr 50, 760–763. [PubMed: 15299374]

Delogu R, Battistone A, Buttinelli G, Fiore S, Fontana S, Amato C, Cristiano K, Gamper S, Simeoni J, Frate R, et al. (2018). Poliovirus and other enteroviruses from environmental surveillance in Italy, 2009–2015. Food Environ. Virol 10, 333–342. [PubMed: 29948963]

Dunne JL, Richardson SJ, Atkinson MA, Craig ME, Dahl-Jørgensen K, Flodström-Tullberg M, Hyöty H, Insel RA, Lernmark Å, Lloyd RE, et al. (2019). Rationale for enteroviral vaccination and antiviral therapies in human type 1 diabetes. Diabetologia 62, 744–753. [PubMed: 30675626]

Emsley P, Lohkamp B, Scott WG, and Cowtan K (2010). Features and development of coot. Acta Crystallogr. D Biol. Crystallogr 66, 486–501. [PubMed: 20383002]

Excoffon KJDA (2020). The coxsackievirus and adenovirus receptor: virological and biological beauty. FEBS Lett. 594, 1828–1837. [PubMed: 32298477]

Fricks CE, and Hogle JM (1990). Cell-induced conformational change in poliovirus: externalization of the amino terminus of VP1 is responsible for liposome binding. J. Virol 64, 1934–1945. [PubMed: 2157861]

Gouet P, Robert X, and Courcelle E (2003). ESPript/ENDscript: extracting and rendering sequence and 3D information from atomic structures of proteins. Nucleic Acids Res. 31, 3320–3323. [PubMed: 12824317]

Greve JM, Davis G, Meyer AM, Forte CP, Yost SC, Marlor CW, Kamarck ME, and McClelland A (1989). The major human rhinovirus receptor is ICAM-1. Cell 56, 839–847. [PubMed: 2538243]

Hayakawa T, Nakano Y, Hayakawa K, Yoshimatu H, Hori Y, Yamanishi K, Yamanishi H, Ota T, and Fujimoto T (2019). Fulminant type 1 diabetes mellitus associated with coxsackievirus type B1 infection during pregnancy: a case report. J. Med. Case Rep 13, 186. [PubMed: 31215492]

He M, Xu L, Zheng Q, Zhu R, Yin Z, Zha Z, Lin Y, Yang L, Huang Y, Ye X, et al. (2020). Identification of antibodies with non-overlapping neutralization sites that target coxsackievirus A16. Cell Host Microbe 27, 249–261.e5. [PubMed: 32027857]

He Y, Chipman PR, Howitt J, Bator CM, Whitt MA, Baker TS, Kuhn RJ, Anderson CW, Freimuth P, and Rossmann MG (2001). Interaction of coxsackievirus B3 with the full length coxsackievirus-adenovirus receptor. Nat. Struct. Biol 8, 874–878. [PubMed: 11573093]

Hodik M, Anagandula M, Fuxe J, Krogvold L, Dahl-Jørgensen K, Hyöty H, Sarmiento L, Frisk G, and POD-V Consortium. (2016). Coxsackie-adenovirus receptor expression is enhanced in pancreas from patients with type 1 diabetes. BMJ Open Diabetes Res. Care 4, e000219.

Huber S, and Ramsingh AI (2004). Coxsackievirus-induced pancreatitis. Viral Immunol. 17, 358–369. [PubMed: 15357902]

Hyöty H, Leon F, and Knip M (2018). Developing a vaccine for type 1 diabetes by targeting coxsackievirus B. Vaccines 17, 1071–1083.

Kallewaard NL, Zhang L, Chen JW, Guttenberg M, Sanchez MD, and Bergelson JM (2009). Tissue-specific deletion of the coxsackievirus and adenovirus receptor protects mice from virus-induced pancreatitis and myocarditis. Cell Host Microbe 6, 91–98. [PubMed: 19616768]

Kimanius D, Forsberg BO, Scheres SH, and Lindahl E (2016). Accelerated cryo-EM structure determination with parallelisation using GPUs in RELION-2. eLife 5, e18722. [PubMed: 27845625]

Krogvold L, Edwin B, Buanes T, Frisk G, Skog O, Anagandula M, Korsgren O, Undlien D, Eike MC, Richardson SJ, et al. (2015). Detection of a low-grade enteroviral infection in the islets of langerhans of living patients newly diagnosed with type 1 diabetes. Diabetes 64, 1682–1687. [PubMed: 25422108]

Li Q, Yafal AG, Lee YM, Hogle J, and Chow M (1994). Poliovirus neutralization by antibodies to internal epitopes of VP4 and VP1 results from reversible exposure of these sequences at physiological temperature. J. Virol 68, 3965–3970. [PubMed: 7514682]

Livak KJ, and Schmittgen TD (2001). Analysis of relative gene expression data using real-time quantitative PCR and the 2(-delta delta C(T)) method. Methods 25, 402–408. [PubMed: 11846609]

Lugo D, and Krogstad P (2016). Enteroviruses in the early 21st century: new manifestations and challenges. Curr. Opin. Pediatr 28, 107–113. [PubMed: 26709690]

Marsh M, and Helenius A (2006). Virus entry: open sesame. Cell 124, 729–740. [PubMed: 16497584]

Mendelsohn CL, Wimmer E, and Racaniello VR (1989). Cellular receptor for poliovirus: molecular cloning, nucleotide sequence, and expression of a new member of the immunoglobulin superfamily. Cell 56, 855–865. [PubMed: 2538245]

Nishimura Y, Shimojima M, Tano Y, Miyamura T, Wakita T, and Shimizu H (2009). Human P-selectin glycoprotein ligand-1 is a functional receptor for enterovirus 71. Nat. Med 15, 794–797. [PubMed: 19543284]

Organtini LJ, Makhov AM, Conway JF, Hafenstein S, and Carson SD (2014). Kinetic and structural analysis of coxsackievirus B3 receptor interactions and formation of the A-particle. J. Virol 88, 5755–5765. [PubMed: 24623425]

Panjwani A, Strauss M, Gold S, Wenham H, Jackson T, Chou JJ, Rowlands DJ, Stonehouse NJ, Hogle JM, and Tuthill TJ (2014). Capsid protein VP4 of human rhinovirus induces membrane permeability by the formation of a size-selective multimeric pore. PLoS Pathog. 10, e1004294. [PubMed: 25102288]

Pauwels S, De Moor B, Stas K, Magerman K, Gyssens IC, Van Ranst M, and Cartuyvels R (2012). Coxsackievirus B1 peritonitis in a patient treated with continuous ambulatory peritoneal dialysis: a case report and brief review of the literature. Clin. Microbiol. Infect 18, E431–E434. [PubMed: 22882320]

Pettersen EF, Goddard TD, Huang CC, Couch GS, Greenblatt DM, Meng EC, and Ferrin TE (2004). UCSF Chimera–a visualization system for exploratory research and analysis. J. Comp. Chem 25, 1605–1612. [PubMed: 15264254]

Plevka P, Perera R, Cardosa J, Kuhn RJ, and Rossmann MG (2012). Crystal structure of human enterovirus 71. Science 336, 1274. [PubMed: 22383808]

Pollack A, Kontorovich AR, Fuster V, and Dec GW (2015). Viral myocarditis–diagnosis, treatment options, and current controversies. Nat. Rev. Cardiol 12, 670–680. [PubMed: 26194549]

Punjani A, Rubinstein JL, Fleet DJ, and Brubaker MA (2017). cryoSPARC: algorithms for rapid unsupervised cryo-EM structure determination. Nat. Methods 14, 290–296. [PubMed: 28165473]

Ren J, Wang X, Hu Z, Gao Q, Sun Y, Li X, Porta C, Walter TS, Gilbert RJ, Zhao Y, et al. (2013). Picornavirus uncoating intermediate captured in atomic detail. Nat. Commun 4, 1929. [PubMed: 23728514]

Richardson SJ, and Morgan NG (2018). Enteroviral infections in the pathogenesis of type 1 diabetes: new insights for therapeutic intervention. Curr. Opin. Pharmacol 43, 11–19. [PubMed: 30064099]

Rossmann MG, Arnold E, Erickson JW, Frankenberger EA, Griffith JP, Hecht HJ, Johnson JE, Kamer G, Luo M, and Mosser AG (1985). Structure of a human common cold virus and functional relationship to other picornaviruses. Nature 317, 145–153. [PubMed: 2993920]

Scheres SH, and Chen S (2012). Prevention of overfitting in cryo-EM structure determination. Nat. Methods 9, 853–854. [PubMed: 22842542]

Seiradake E, Lortat-Jacob H, Billet O, Kremer EJ, and Cusack S (2006). Structural and mutational analysis of human Ad37 and canine adenovirus 2 fiber heads in complex with the D1 domain of coxsackie and adenovirus receptor. J. Biol. Chem 281, 33704–33716. [PubMed: 16923808]

Staring J, van den Hengel LG, Raaben M, Blomen VA, Carette JE, and Brummelkamp TR (2018). KREMEN1 is a host entry receptor for a Major Group of enteroviruses. Cell Host Microbe 23, 636–643.e5. [PubMed: 29681460]

Strauss M, Filman DJ, Belnap DM, Cheng N, Noel RT, and Hogle JM (2015). Nectin-like interactions between poliovirus and its receptor trigger conformational changes associated with cell entry. J. Virol 89, 4143–4157. [PubMed: 25631086]

Sun Y, Watters K, Hill MG, Fang Q, Liu Y, Kuhn RJ, Klose T, Rossmann MG, and Palmenberg AC (2020). Cryo-EM structure of rhinovirus C15a bound to its cadherin-related protein 3 receptor. Proc. Natl. Acad. Sci. USA 117, 6784–6791. [PubMed: 32152109]

Swint-Kruse L, and Brown CS (2005). Resmap: automated representation of macromolecular interfaces as two-dimensional networks. Bioinformatics 21, 3327–3328. [PubMed: 15914544]

Tavakoli NP, Wang H, Nattanmai S, Dupuis M, Fusco H, and Hull R (2008). Detection and typing of enteroviruses from CSF specimens from patients diagnosed with meningitis/encephalitis. J. Clin. Virol 43, 207–211. [PubMed: 18692435]

Towbin JA, Lowe AM, Colan SD, Sleeper LA, Orav EJ, Clunie S, Messere J, Cox GF, Lurie PR, Hsu D, et al. (2006). Incidence, causes, and outcomes of dilated cardiomyopathy in children. JAMA 296, 1867–1876. [PubMed: 17047217]

Vehik K, Lynch KF, Wong MC, Tian X, Ross MC, Gibbs RA, Ajami NJ, Petrosino JF, Rewers M, Toppari J, et al. (2019). Prospective virome analyses in young children at increased genetic risk for type 1 diabetes. Nat. Med 25, 1865–1872. [PubMed: 31792456]

Verdino P, Witherden DA, Havran WL, and Wilson IA (2010). The molecular interaction of CAR and JAML recruits the central cell signal transducer PI3K. Science 829, 1210–1214.

Walter TS, Ren J, Tuthill TJ, Rowlands DJ, Stuart DI, and Fry EE (2012). A plate-based high-throughput assay for virus stability and vaccine formulation. J. Virol. Methods 185, 166–170. [PubMed: 22744000]

Wang X, Peng W, Ren J, Hu Z, Xu J, Lou Z, Li X, Yin W, Shen X, Porta C, et al. (2012). A sensor-adaptor mechanism for enterovirus uncoating from structures of EV71. Nat. Struct. Mol. Biol 19, 424–429. [PubMed: 22388738]

Wang X, Zhu L, Dang M, Hu Z, Gao Q, Yuan S, Sun Y, Zhang B, Ren J, Kotecha A, et al. (2017). Potent neutralization of hepatitis A virus reveals a receptor mimic mechanism and the receptor recognition site. Proc. Natl. Acad. Sci. USA 114, 770–775. [PubMed: 28074040]

Xiao C, and Rossmann MG (2007). Interpretation of electron density with stereographic roadmap projections. J. Struct. Biol 158, 182–187. [PubMed: 17116403]

Xu L, He D, Li Z, Zheng J, Yang L, Yu M, Yu H, Chen Y, Que Y, Shih JWK, et al. (2014). Protection against lethal enterovirus 71 challenge in mice by a recombinant vaccine candidate containing a broadly cross-neutralizing epitope within the VP2 EF loop. Theranostics 4, 498–513. [PubMed: 24669278]

Xu L, Zheng Q, Li S, He M, Wu Y, Li Y, Zhu R, Yu H, Hong Q, Jiang J,et al. (2017). Atomic structures of coxsackievirus A6 and its complex with a neutralizing antibody. Nat. Commun 8, 505. [PubMed: 28894095]

Yamayoshi S, Yamashita Y, Li J, Hanagata N, Minowa T, Takemura T, and Koike S (2009). Scavenger receptor B2 is a cellular receptor for enterovirus 71. Nat. Med 15, 798–801. [PubMed: 19543282]

Yan X, Sinkovits RS, and Baker TS (2007). AUTO3DEM–an automated and high throughput program for image reconstruction of icosahedral particles. J. Struct. Biol 157, 73–82. [PubMed: 17029842]

Zhang K (2016). Gctf: real-time CTF determination and correction. J. Struct. Biol 193, 1–12. [PubMed: 26592709]

Zhang P, Mueller S, Morais MC, and Bator CM (2008). Crystal structure of CD155 and electron microscopic studies of its complexes with polioviruses. Proc. Natl. Acad. Sci. USA 105, 18284–18289. [PubMed: 19011098]

Zhao X, Zhang G, Liu S, Chen X, Peng R, Dai L, Qu X, Li S, Song H, Gao Z, et al. (2019). Human neonatal Fc receptor is the cellular uncoating receptor for enterovirus B. Cell 177, 1553–1565.e16. [PubMed: 31104841]

Zhao Y, Zhou D, Ni T, Karia D, Kotecha A, Wang X, Rao Z, Jones EY, Fry EE, Ren J, and Stuart DI (2020). Hand-foot-and-mouth disease virus receptor KREMEN1 binds the canyon of Coxsackie Virus A10. Nat. Commun 11, 38, 38. [PubMed: 31911601]

Zheng Q, Zhu R, Xu L, He M, Yan X, Liu D, Yin Z, Wu Y, Li Y, Yang L, et al. (2019). Atomic structures of enterovirus D68 in complex with two monoclonal antibodies define distinct mechanisms of viral neutralization. Nat. Microbiol 4, 124–133. [PubMed: 30397341]

Zheng SQ, Palovcak E, Armache JP, Verba KA, Cheng Y, and Agard DA (2017). MotionCor2: anisotropic correction of beam-induced motion for improved cryo-electron microscopy. Nat. Methods 14, 331–332. [PubMed: 28250466]

Zhou D, Zhao Y, Kotecha A, Fry EE, Kelly JT, Wang X, Rao Z, Rowlands DJ, Ren J, and Stuart DI (2019). Unexpected mode of engagement between enterovirus 71 and its receptor SCARB2. Nat. Microbiol 4, 414–419. [PubMed: 30531980]

Zhu R, Xu L, Zheng Q, Cui Y, Li S, He M, Yin Z, Liu D, Li S, Li Z, et al. (2018). Discovery and structural characterization of a therapeutic antibody against coxsackievirus A10. Sci. Adv 4, eaat7459. [PubMed: 30255146]

Highlights

- Group B coxsackievirus uncoating is mediated by its receptor CAR under neutral conditions
- High-resolution cryoEM structures unveiled mechanism of CAR-initiated virus uncoating
- CAR-guided discovery identified therapeutic antibody, 5F5, against CVB infection
- 5F5 blocked receptor binding and triggered virion disruption via functional mimicry

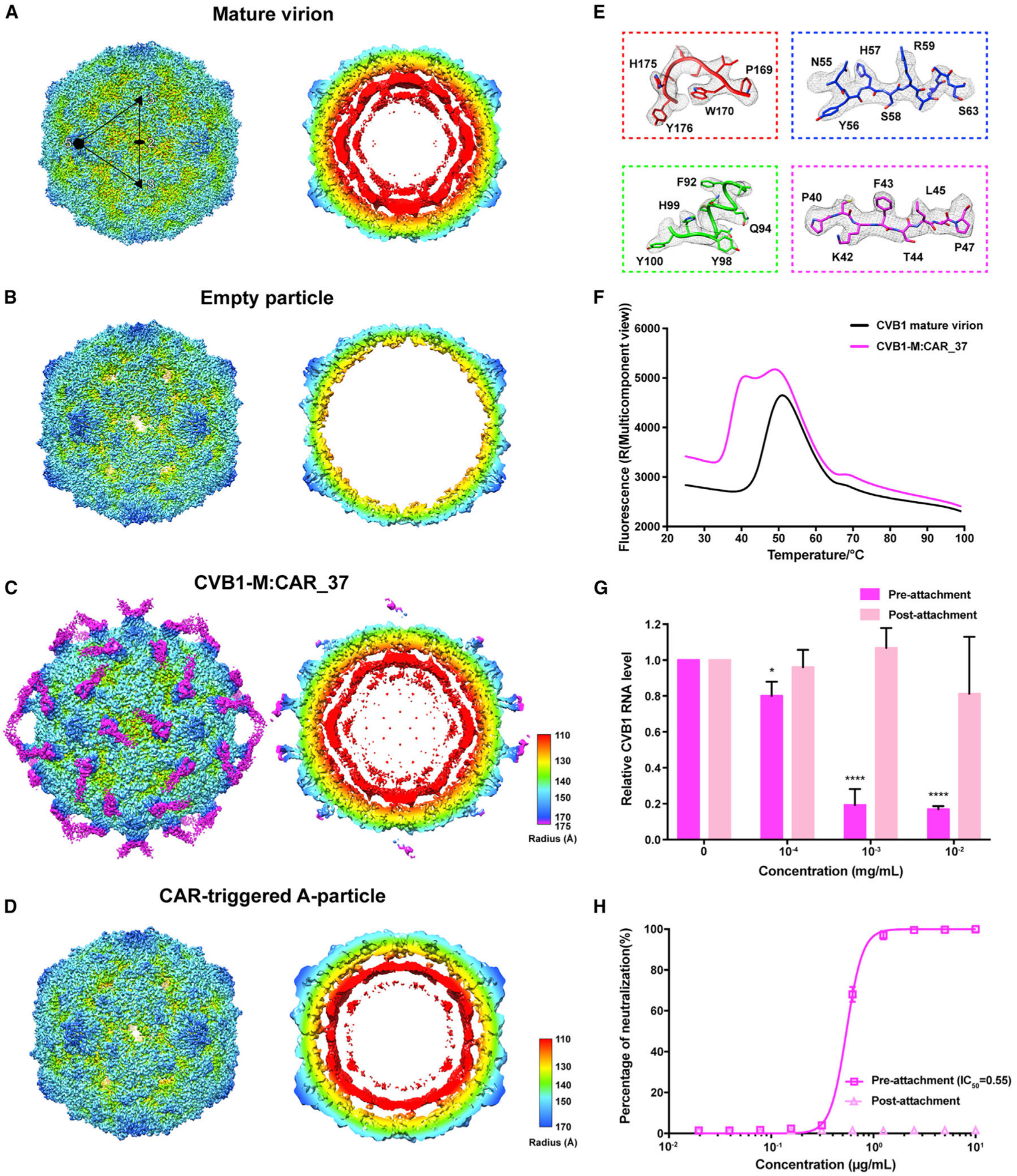

Figure 1. Structure determination and characterization of CVB1 particles before and after binding of CAR

(A–D) Radially colored surface views of the cryoEM density maps of the CVB1 mature virion (A), the empty particle (B), the CVB1-M:CAR_37 complex (C) and the CAR-triggered A-particle (D), examined along a icosahedral 2-fold axis from outside (left panels) and as a central slab of 25-Å thickness (right panels). One icosahedral asymmetric unit is marked by a black triangle in (A).

(E) Quality of the structure of CVB1-M:CAR_37 as illustrated by superposition of selected regions of the density map (gray) and atomic models of VP1 (blue), VP2 (green), VP3 (red), and CAR (magenta), respectively.

(F) PaSTRy assay of CVB1 mature virion and its complex with CAR. Fluorescence traces are shown for the CVB1 mature virion (black line) and its complex with CAR (magenta line). The experiments were repeated independently in triplicate and one representative result is shown.

(G) Amount of cell-bound CVB1 viruses based on the relative viral RNA levels detected by quantitative real-time RT-PCR in pre-attachment (magenta column) and post-attachment (pink column) assays of CAR. The values are expressed as the mean ± SD. Significance was determined using an unpaired Student's t test. $*p < 0.05$, $****p < 0.0001$.

(H) Percentage of CAR neutralization of virus infection as a function of CAR in pre- (magenta line) and post-attachment (pink line) neutralization assays of CAR. Values are expressed as the mean ± SD. Neutralization efficacy is depicted with IC_{50} values, calculated by nonlinear regression fitting curves using GraphPad Prism version 7.0.

The experiments in (G and H) were repeated in triplicate.

See also Figures S1-S3; Video S1; Table S1.

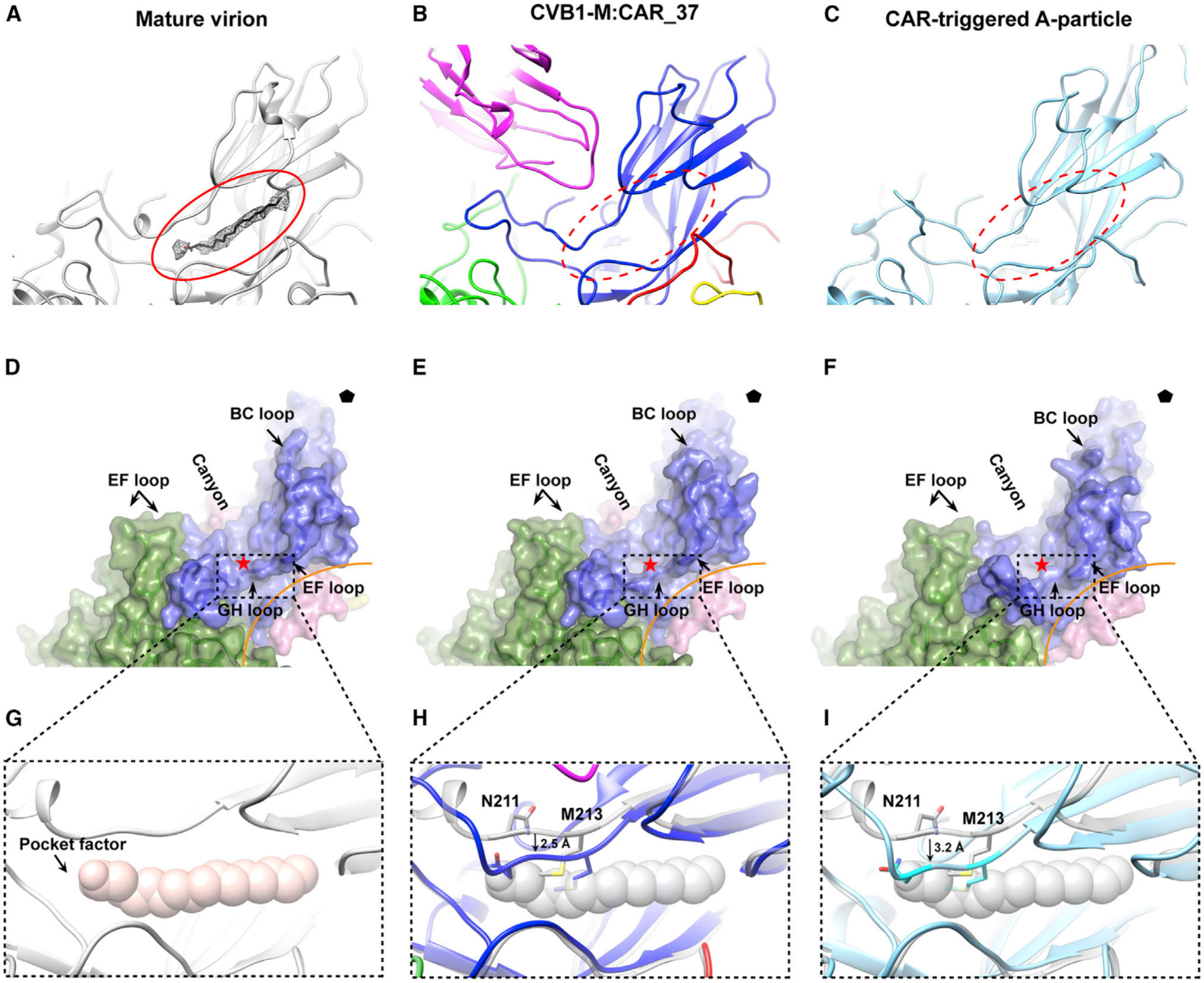

Figure 2. CAR-induced conformational changes in canyon regions and the release of the pocket factor

(A–C) Cartoon views of the hydrophobic pocket and its pocket factor from different CVB1 particles. Pocket factor density is shown at a 2.5-σ contour level and as a gray mesh and is superposed with its atomic model as sticks. Pocket factor is present in the CVB1 mature virion (red oval, ribbon structure) (A), but absent in both the CAR-decorated complex (rainbow colored) (B) and CAR-triggered A-particle (cyan) (C), as indicated by the red dashed ovals at the same positions in (A). The capsid proteins and the bound CAR of the CAR-decorated complex are colored blue (VP1), green (VP2), red (VP3), yellow (VP4), and magenta (CAR), respectively.

(D–F) Surface representations of the protomers of the CVB1 mature virion (D), CAR-decorated complex (E), and CAR-triggered A-particle (F). The VP1 BC, EF, and GH loops, and the VP2 EF loop—comprising the hydrophobic pocket—are marked, and the canyon region is highlighted by a red star.

(G–I) Close-up views of the capsid proteins surrounding the pocket factor from different particles. The internal pocket factor is shown in surface mode and colored in light salmon in

(G). Superpositions of the protomers between the CVB1 mature virion (gray) and the CAR-decorated complex (rainbow colored) (H) or CAR-triggered A-particle (cyan) (I) are shown. The residues potentially involved in “crowding out” the pocket factor are shown in stick form and colored by elements.
See also Figure S3; Video S2.

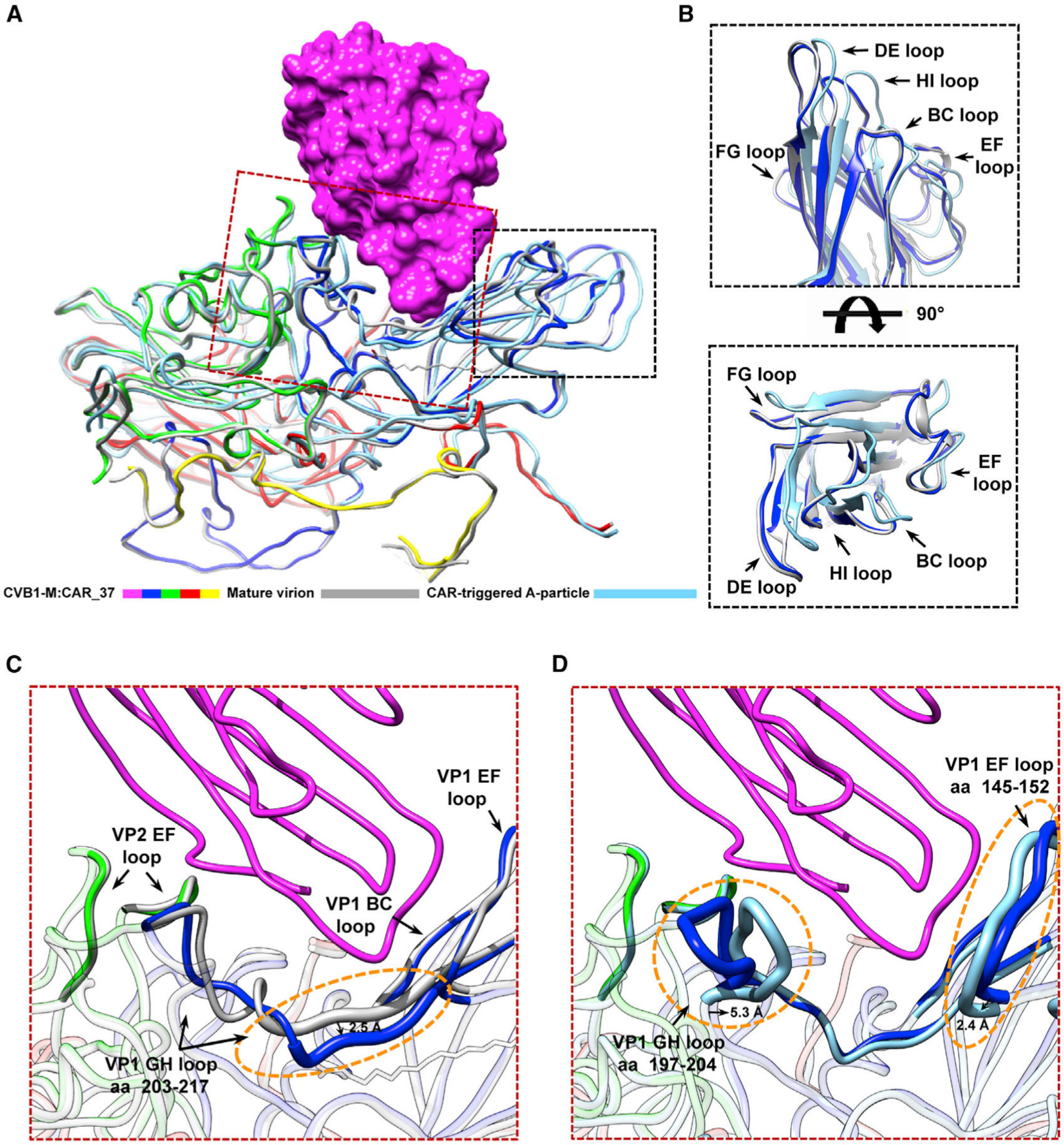

Figure 3. Structural comparison of mature virion, the CAR-decorated complex, and the A-particle showing details of the CAR-mediated uncoating process

(A–D) Superposition of the protomers of the CAR-decorated complex, the mature virion, and the CAR-triggered A-particle. The receptor is shown in surface representation (magenta) and the capsid proteins in cartoon representation. The color scheme is as in Figure 2. Structural differences among the three particles are mainly located on the VP1 loops (BC, DE, EF, FG, and HI loops) close to 5-fold axis (B) and the VP1 GH loops around the canyon (C and D). Close-up views of the CAR-binding sites of the CAR-decorated complex compared with those of the mature virion (C) and the CAR-triggered A-particle (D). The regions on the capsid of the CAR-decorated complex are highlighted, and the key loops involved in significant conformational changes are shown in bold cartoon representation (orange dashed ovals).

See also Figure S4; Video S2.

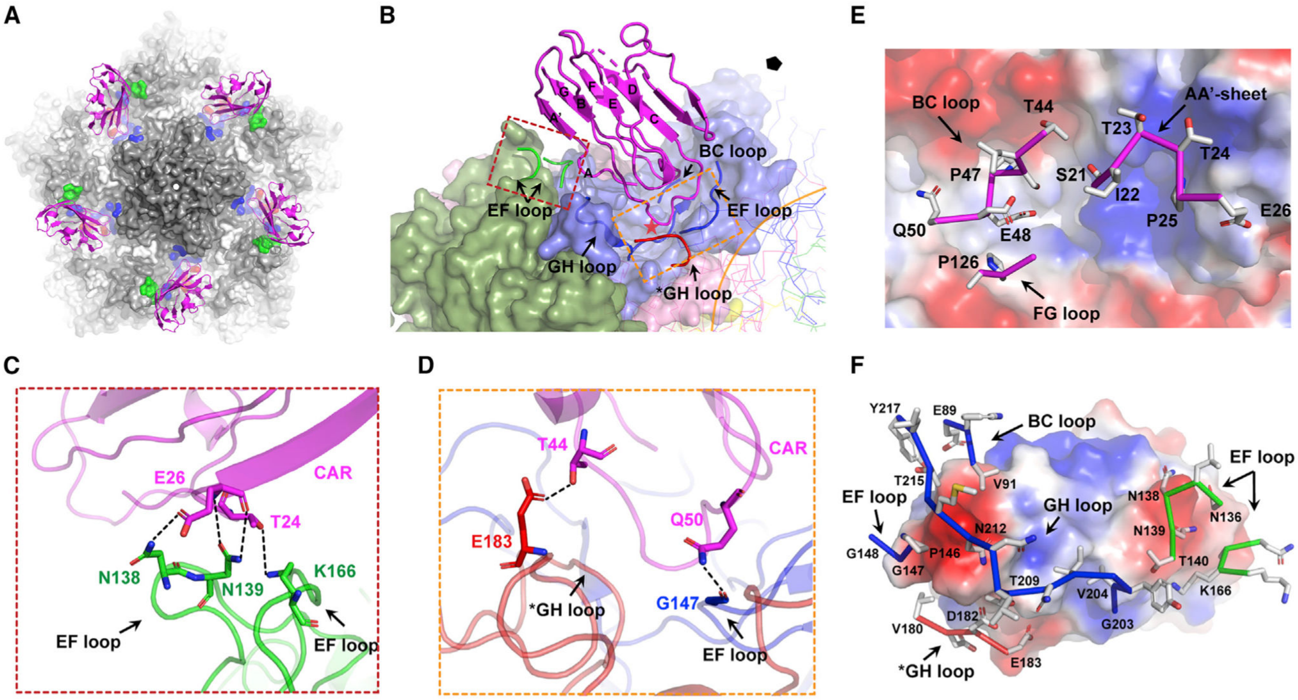

Figure 4. Molecular interactions between CVB1 and CAR

(A) Outside view of a pentamer with five CAR receptors engaged in the canyon region around the icosahedral 5-fold axis. The capsid proteins are shown in surface representation (gray) and the bound CAR as cartoon representation (magenta). The footprints of CAR on VP1–VP3 are colored blue, green, and red, respectively.

(B–D) Interactions between CVB1 and CAR. The region in the CAR-decorated CVB1 surrounding one bound CAR is shown in (B). CAR and its binding loops on the capsid are shown as ribbon and the rest of the main protomer of CVB1 involved in the interaction is shown in surface representation and the adjacent protomer in ribbon mode. The VP3 GH loop from the adjacent protomer involved in interaction is identified by an asterisk and the hydrophobic pocket by a red star. The color scheme is as in Figure 2. The interaction details and potential hydrogen bonds (marked by black dashed lines) are magnified in parts (C) and (D).

(E and F) The contact areas on CVB1 shown as an electrostatic surface (±50 kTe^{-1}; blue, positive; red, negative), CAR as sticks (E), and vice versa (F).

See also Figure S5.

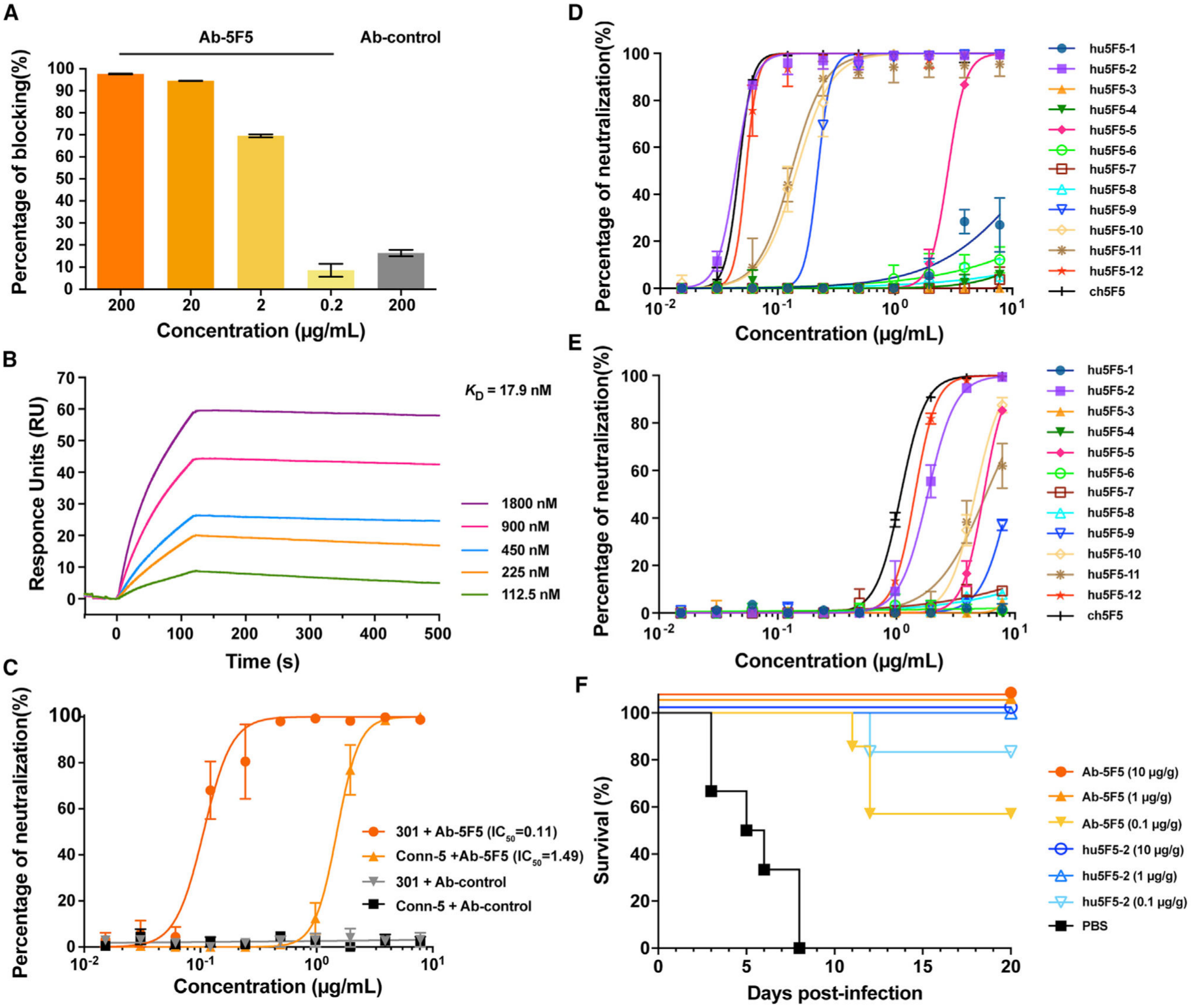

Figure 5. Characterization of anti-CVB1 neutralizing antibody 5F5

(A) Blocking efficiency of nAb 5F5 against CAR binding. The percentage of blocked CAR binding is expressed as the mean ± SD. Binding of CAR to the CVB1 mature virions is significantly blocked by 5F5 concentrations over 2 μg mL^{-1}.

(B) Affinity of nAb 5F5 to the CVB1 mature virions quantified by SPR assay and shown as the response units over time for several antibody concentrations. The binding affinity of nAb 5F5 for the CVB1 mature virions as revealed by a K_D (equilibrium dissociation constant, $K_D = K_d/K_a$) value of 17.9 nM ($K_d = 1.28 \times 10^{-4}$ s^{-1}, $K_a = 7.13 \times 10^3$ $M^{-1}s^{-1}$). The experiments were repeated independently thrice and the 5F5 bound to CVB1 virions with an affinity of 22.6 ± 5.8 nM.

(C) Cross-neutralizing efficacy of nAb 5F5 against two strains of CVB1 (strains 301 and Conn-5) as by *in vitro* micro-neutralization assay, shown as the percentage of neutralized virus at different concentrations of antibodies (Ab). The values are expressed as the mean ± SD. The neutralization efficacy value, IC_{50}, was calculated by nonlinear regression fitting curves using GraphPad Prism version 7.0 and the data are shown in parentheses.

(D) Neutralizing efficacy of ch5F5 or twelve humanized 5F5 antibodies against CVB1 strain 301 as by *in vitro* micro-neutralization assay, shown as the percentage of neutralized virus at different concentrations of antibodies. The values are expressed as the mean ± SD.
(E) Neutralizing efficacy of ch5F5 or twelve humanized 5F5 antibodies against CVB1 strain Conn-5 as by *in vitro* micro-neutralization assay, shown as the percentage of neutralized virus at different concentrations of antibodies. The values are expressed as the mean ± SD.
(F) *In vivo* animal protective efficacy of nAb 5F5 or hu5F5-2 against CVB1 infection. 1-day-old mice were first challenged with CVB1 and then different doses of antibodies were administered 12 h post infection. Mice were monitored daily for survival after inoculation. Mice in the control group were treated with PBS. The experiments in (A–F) were repeated independently at least twice and those shown in (B) and (F) are one representative result.

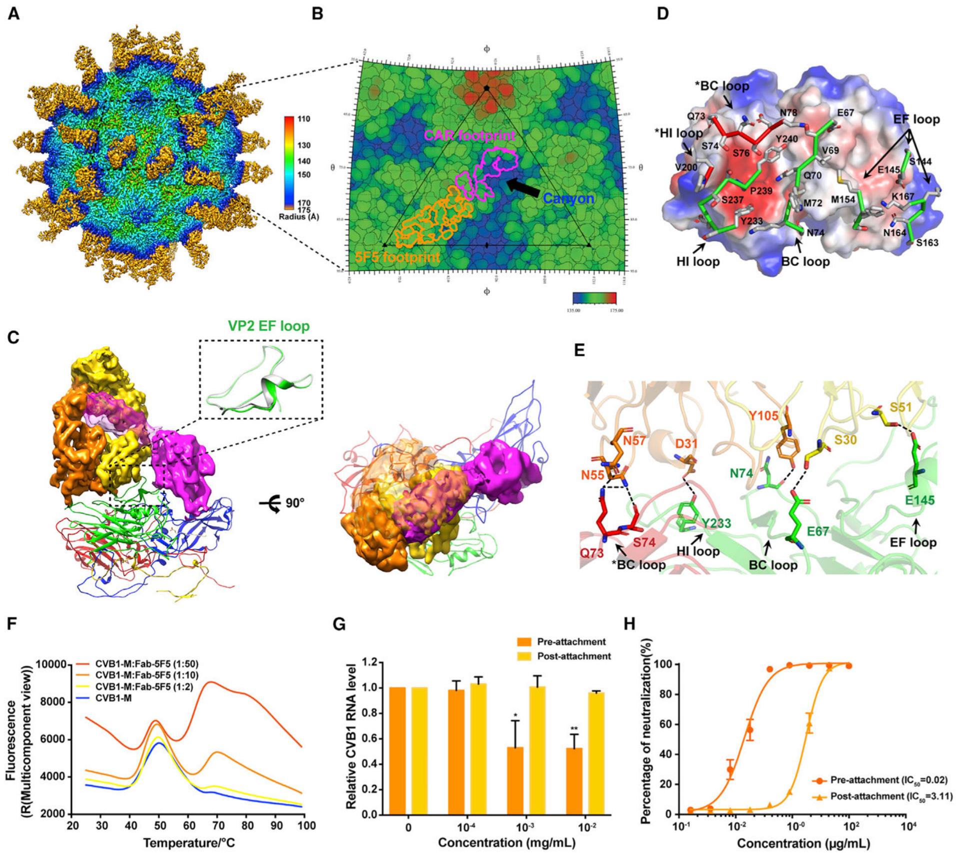

Figure 6. CryoEM structure of CVB1-M:5F5 and neutralizing mechanism of nAb 5F5

(A) Radially colored surface views down the icosahedral 2-fold axis of the cryoEM density map of CVB1-M:5F5.

(B) Roadmap of the footprints of nAb 5F5 (orange circle) and CAR (magenta circle) on the virus surface.

(C) Assumed binding modality of nAb 5F5 and CAR to CVB1 mature virion (CVB1-M), illustrated according to the cryoEM structures of CVB1-M:CAR_37 and CVB1-M:5F5. Viral capsid proteins VP1–VP4 are shown as ribbons in blue, green, red, and yellow, respectively. The bound nAb 5F5 (heavy chain, orange; light chain, yellow) and CAR (magenta) are represented in surface representation. 5F5 binding induced minor conformational changes in the VP2 EF loop, highlighted by the dashed square.

(D) The contact areas on the Fab shown as electrostatic surface (±50 kTe^{-1}; blue, positive; red, negative) and the capsid proteins of CVB1 shown as sticks.

(E) Close-up view of the interface details and potential hydrogen bonds (marked by black dashed lines) between the capsid proteins and either the heavy or light chain of Fab-5F5. The color scheme is as in (C).

(F) PaSTRy assay of CVB1 mature virion (CVB1-M) and its complex with Fab-5F5 at different antibody concentrations. The experiments were repeated independently in triplicate and the result of one representative is shown.

(G) The amount of cell-bound CVB1 virus as measured by quantitative real-time RT-PCR in pre- and post-attachment assays of nAb 5F5. The values are expressed as the mean ± SD. Significance was determined using unpaired Student's t test. $*p < 0.05$, $**p < 0.01$.

(H) Neutralization assay showing percentage of virus neutralization as a function of concentration in pre- and post-attachment assays of nAb 5F5. Values are expressed as the mean ± SD. The neutralization efficacy is depicted as IC_{50} values, calculated by nonlinear regression fitting curves using GraphPad Prism version 7.0.

The experiments in (G) and (H) were repeated in triplicate.

See also Figures S1 and S2; Video S3; Table S1.

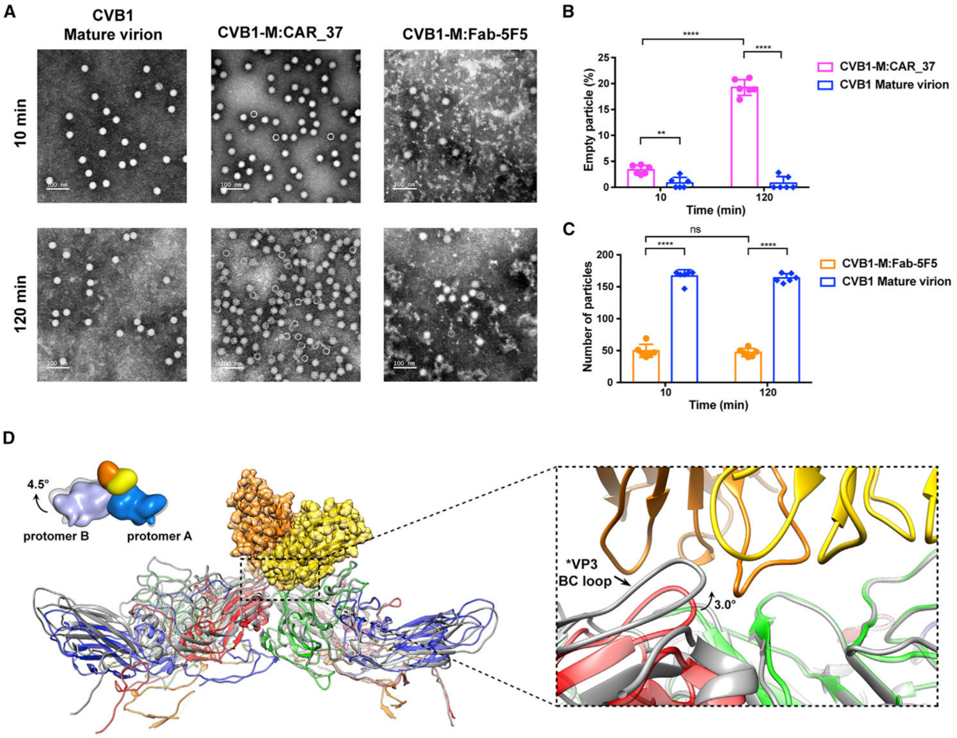

Figure 7. Efficient uncoating effect of CAR and capsid-disruption potential of 5F5

(A) Representative negative-staining TEM images of CVB1 before and after binding of CAR or nAb 5F5. Samples were incubated at 37°C for 10 or 120 min as indicated.

(B) Percentage of CAR-induced empty particles in each group was counted manually and the significance was determined by Tukey’s multiple comparisons test. Values are expressed as the mean ± SD. $**p < 0.01$, $****p < 0.0001$.

(C) Total particle number of the mature virions alone or following incubation with 5F5 were counted manually, with significance determined using an unpaired Student’s t test. Values are expressed as the mean ± SD. $****p < 0.0001$. ns, non-significant.

(D) Superposition of two adjacent protomers (protomer A, right; protomer B, left) of CVB1-M:5F5 (rainbow-colored ribbon) and the A-particle (gray ribbon) with the two variable domains (orange and yellow) of one Fab fragment shown as space-filling representation. The color scheme is as in Figure 2. The diagram in the upper left corner depicts the structural discrepancy between the two adjacent protomers, with aglobal rotation of 4.5° for protomer B. The epitope regions with the most significant conformational changes between the two models are highlighted with magnified views in the dashed boxes, in which 5F5 is also shown as ribbon.

See also Figures S6 and S7.

KEY RESOURCES TABLE

REAGENT or RESOURCE	SOURCE	IDENTIFIER
Antibodies		
Anti-CVB1 mouse monoclonal antibody 5F5	This study	N/A
anti-CVB1 mouse monoclonal antibody 8A10	This study	N/A
Anti-CVA10 mouse monoclonal antibody Ab-control	This study	N/A
HRP-conjugated Goat anti-Human IgG	This study	N/A
Bacterial and virus strains		
CVB1 301 strain	This study	GenBank: MT129657
CVB1 Conn-5 strain	ATCC	Cat# VR-28™
DH5α Competent Cell	TianGen	Cat# CB101
Chemicals, peptides, and recombinant proteins		
Human CAR soluble protein	This study	GenBank: P78310
SYTO® 9	Thermo Fisher	Cat# S34854
Polyethylenimine, PEI	Polysciences	Cat# 23966-2
Critical commercial assays		
NuPAGE™ 4-12% Bis-Tris Protein Gels	Thermo Fisher	Cat# NP0321BOX
AT Protein A Diamond	Bestchrom	Cat# AA0273
DEAE-5PW (20)	TOSOH	Cat# 14711
Series S Sensor Chip Protein G	GE Healthcare	Cat# 29179315
EndoFree Maxi Plasmid Kit	TianGen	Cat# DP117
QIAamp Mini viral RNA Extraction Kit	Qiagen	Cat# 52904
Deposited data		
CryoEM structure CVB1-M	This study	EMBD-30805, PDB:7DPF
CryoEM structure CVB1-E	This study	EMBD-30806, PDB:7DPG
CryoEM structure CVB1-M:CAR_4	This study	EMBD-30812, PDB:7DPZ
CryoEM structure CVB1-M:CAR_37	This study	EMBD-30813, PDB:7DQ1
CryoEM structure CVB1-A	This study	EMBD-30814, PDB:7DQ4
CryoEM structure CVB1-M:5F5	This study	EMBD-30815, PDB:7DQ7
Experimental models: cell lines		
RD cells	ATCC	Cat# CCL-136
Myeloma cells (Sp2/0)	This study	N/A
Expi293F™ cells	Thermo Fisher	Cat# A14528
Experimental models: organisms/strains		
BALB/c mice	Slac Laboratiry Animal Co., shanghai, China	N/A
Oligonucleotides		
Primers: CVB1-F: CTACCACTCACGGTCCGAATCGT; CVB1-R: TGAGTTRTTRGTGTATGTGGCATAGT; CVB1-P: FAM-CCTGTGCCGGTCTGCCTGTG-BHQ-2	This study	N/A
Primers: hGAPDH-F: TATTGGGCGCCTGGTC; hGAPDH-R: GACGGTGCCATGGAATT; hGAPDH-P: HEX-TTAACTCTGGTAAAGTGGATATTGTTGCC-BHQ-2	This study	N/A

REAGENT or RESOURCE	**SOURCE**	**IDENTIFIER**
Recombinant DNA		
pTT5-hCAR-D1-D2-Fc	This study	N/A
Software and algorithms		
Prism 7.0	GraphPad Software	N/A
BIAcore 8K Evaluation software	GE Healthcare	N/A
Accelrys Discovery Studio software	BIOVIA	https://www.3dsbiovia.com/products/collaborative-science/biovia-discovery-studio/
MotionCor2	(Zheng et al., 2017)	N/A
Gctf	(Zhang, 2016)	N/A
Gautomatch	MRC	https://www2.mrc-lmb.cam.ac.uk/research/locally-developed-software/zhang-software/#gauto
RELION 2.1	(Kimanius et al., 2016)	N/A
ResMap	(Swint-Kruse and Brown, 2005)	N/A
AUTO3DEM	(Yan et al., 2007)	N/A
Chimera	(Pettersen et al., 2004)	N/A
Pymol	Schrödinger, LLC	https://pymol.org/2/
cryoSPARC 2.4.2	(Punjani et al., 2017)	N/A
COOT	(Emsley et al., 2010)	N/A
PHENIX	(Adams et al., 2010)	http://phenix-online.org
Molprobity	(Chen et al., 2010)	http://molprobity.biochem.duke.edu
CCP4	(Collaborative Computational Project, Number 4, 1994)	http://www.ccp4.ac.uk
PISA	EMBL-EBI	https://www.ebi.ac.uk/pdbe/pisa/
Rivem	(Xiao and Rossmann, 2007)	N/A
ESPript 3.0	(Gouet et al., 2003)	http://espript.ibcp.fr/ESPript/ESPript/
Other		
Quantifoil R 2/2 Cu grids	Quantifoil	Q2100CR2